

Discovery of Spherules of Likely Extrasolar Composition in the Pacific Ocean Site of the CNEOS 2014-01-08 (IM1) Bolide

Abraham Loeb^{1,2}, Toby Adamson², Sophie Bergstrom², Richard Cloete^{1,2}, Shai Cohen^{2,7}, Kevin Conrad², Laura Domine^{1,2}, Hairuo Fu^{2,3}, Charles Hoskinson², Eugenia Hyung^{2,3}, Stein Jacobsen^{2,3}, Mike Kelly², Jason Kohn², Edwin Lard², Sebastian Lam^{2,4}, Frank Laukien^{2,6}, Jim Lem^{2,5}, Rob McCallum², Rob Millsap², Christopher Parendo^{2,3}, Michail Pataev^{2,3}, Chaitanya Peddeti^{2,4}, Jeff Pugh², Shmuel Samuha^{2,7}, Dimitar Sasselov^{1,2}, Max Schlereth², J.J. Siler², Amir Siraj^{1,2}, Peter Mark Smith², Roald Tagle², Jonathan Taylor², Ryan Weed^{2,4}, Art Wright², and Jeff Wynn²

¹Department of Astronomy, Harvard University, 60 Garden Street, Cambridge, MA 02138, USA

²Interstellar Expedition of the Galileo Project, 60 Garden Street, Cambridge, MA 02138, USA

³Department of Earth and Planetary Sciences, Harvard University, 20 Oxford Street, Cambridge, MA 02138, USA

⁴Department of Nuclear Engineering, UC Berkeley, 4153 Etcheverry Hall, MC 1730, Berkeley, CA 94720, USA

⁵Department of Mining Engineering, PNG University of Technology, Lae 411, Papua New Guinea

⁶Department of Chemistry and Chemical Biology, Harvard University, 12 Oxford Street, Cambridge, MA 02138, USA

⁷Department of Materials Engineering, NRCN, P.O. Box 9001, Beer-Sheva 84190, Israel

Correspondence: Abraham Loeb, Head of the Galileo Project (aloeb@cfa.harvard.edu)

Abstract. We have conducted an extensive towed-magnetic-sled survey during the period 14-28 June, 2023, over the seafloor about 85 km north of Manus Island, Papua New Guinea, and found about 700 spherules of diameter 0.05-1.3 millimeters in our samples, of which 57 were analyzed so far. Approximately 0.26 km² of seafloor was sampled in this survey, centered around the calculated path of the bolide CNEOS 2014-01-08 (IM1) with control areas north and south of that path. The spherules, significantly concentrated along the expected meteor path, were retrieved from seafloor depths ranging between 1.5-2.2 km. Mass spectrometry of 47 spherules near the high-yield regions along IM1's path reveals a distinct extra-solar abundance pattern for 5 of them, while background spherules have abundances consistent with a solar system origin. The unique spherules show an excess of Be, La and U, by up to three orders of magnitude relative to the solar system standard of CI chondrites. These "BeLaU"-type spherules, never seen before, also have very low refractory siderophile elements such as Re. Volatile elements, such as Mn, Zn, Pb, are depleted as expected from evaporation losses during a meteor's airburst. In addition, the mass-dependent variations in ⁵⁷Fe/⁵⁴Fe and ⁵⁶Fe/⁵⁴Fe are also consistent with evaporative loss of the light isotopes during the spherules' travel in the atmosphere. The "BeLaU" abundance pattern is not found in control regions outside of IM1's path and does not match commonly manufactured alloys or natural meteorites in the solar system. This evidence points towards an association of "BeLaU"-type spherules with IM1, supporting its interstellar origin independently of the high velocity and unusual material strength implied from the CNEOS data. We suggest that the "BeLaU" abundance pattern could have originated from a highly differentiated magma ocean of a planet with an iron core outside the solar system or from more exotic sources.

1 Introduction

On 8 January 2014 US government satellite sensors detected three atmospheric detonations in rapid succession about 84 km north of Manus Island, outside the territorial waters of Papua New Guinea (20 km)¹. Analysis of the trajectory suggested an interstellar origin of the causative object CNEOS 2014-01-08: an arrival velocity relative to Earth in excess of $\sim 45 \text{ km s}^{-1}$, and a vector tracked back to outside the plane of the ecliptic (Siraj and Loeb, 2022a). The object's speed relative to the Local Standard of Rest of the Milky-Way galaxy, $\sim 60 \text{ km s}^{-1}$, was higher than 95% of the stars in the Sun's vicinity.

In 2022 the US Space Command issued a formal letter to NASA certifying a 99.999% likelihood that the object was interstellar in origin². Along with this letter, the US Government released the fireball lightcurve as measured by satellites³, which showed three flares separated by a tenth of a second from each other. The bolide broke apart at an unusually low altitude of $\sim 17 \text{ km}$, corresponding to a ram pressure of $\sim 200 \text{ MPa}$. This implied that the object was substantially stronger than any of the other 272 objects in the CNEOS catalog, including the $\sim 5\%$ -fraction of iron meteorites from the solar system (Siraj and Loeb, 2022b). Calculations of the fireball light energy suggest that about 500 kg of material was ablated by the fireball and converted into ablation spherules with a small efficiency (Tillinghast-Raby et al., 2022). The fireball path was localized to a 1 km-wide strip based on the delay in arrival time of the direct and reflected sound waves to a seismometer located on Manus Island (Siraj and Loeb, 2023).

2 Material Acquisition

An international expedition was organized and funded by a private contribution to search for remnants of the bolide, labeled hereafter IM1. The expedition was mounted from Port Moresby, Papua New Guinea (PNG), and utilized a 40-meter catamaran workboat, the M/V Silver Star. A 200-kg sled was used with 300 neodymium magnets mounted on both of its sides and video cameras mounted on the tow-halter (see Figure 1). After several experimental runs, the sled was observed to be 'kiting' above the sea floor. To mitigate the kiting effect, 50 kg of lead were added to the sled. Furthermore, the presence of heterogeneous surface currents and wind forces necessitated complex navigation strategies due to their effect on the vessel's maneuvering. Therefore, we systematically analyzed the seafloor current, enabling the alignment of the sled's trajectory with the prevailing current.

Following this, the sled was towed for an average of ~ 8 hours per run, retrieved and the material was then processed. This process was repeated 26 times over a period of fourteen days. Several of these 'run-tracks' were obtained from areas beyond the predefined target zone, acting as controls for the experiment. We estimate that approximately 0.26 km^2 were sampled in the target area.

¹https://www.un.org/depts/los/LEGISLATIONANDTREATIES/PDFFILES/PNG_1977_Act7.pdf

²<https://lweb.cfa.harvard.edu/~loeb/DoD.pdf>

³<https://lweb.cfa.harvard.edu/~loeb/lightcurve.pdf>

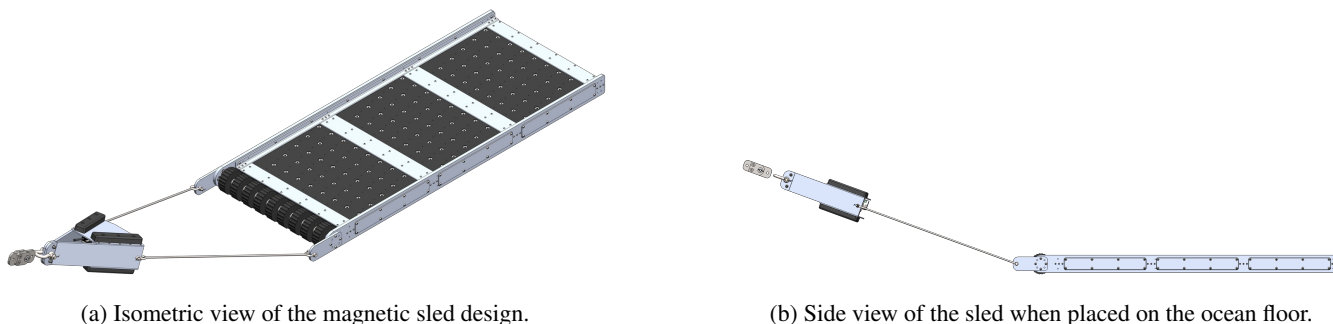


Figure 1. Magnetic sled design. The 200-kg, 1 by 2 meter sled was covered with an array of 300 neodymium magnets on both sides and equipped with video cameras in the metal tow-halter ahead of it, which was anchored by a synthetic cable to a winch on the ship, the M/V Silver Star.

3 Sample Processing

When the material collected from each run of the sled was brought aboard, it was examined carefully, with larger samples (mostly rusted iron) captured in vials for further analysis using X-ray fluorescence (XRF). The fine material collected on the neodymium magnets was then extracted and brought in a wet slurry up to a laboratory set up on the bridge of the vessel for further examination.

There, an initial wet-magnetic separation took place; this was necessary because plankton and foraminifera were commonly entrained in the material attracted to the magnets. Subsequently, both magnetic and non-magnetic separations were processed through sieves and dried. Later an additional dry magnetic separation took place, and these secondary results were scanned with one of three digital microscopes aboard the ship. It was relatively easy to see and extract spherules above a millimeter in diameter with tweezers, but increasingly difficult to isolate below about 100 microns. A more detailed description of the sample-processing scheme is included in Appendix B.

Initial X-ray Fluorescence (XRF) measurements of a few large spherules was attempted while on-board the research vessel using the Bruker CTX. The X-ray beam spot was several times larger than the samples, making backscatter and low absorption challenging. Despite this, reasonable XRF results were obtained for IM1 target area and background spherules.

4 Spherule Count

The spherule count in runs 1-24 is shown in Tables 1 and 2 (with runs 25 & 26 yet to be processed). We use the notation of "IS" (as a short for "Interstellar") to label specific run numbers and SPH to label specific spherule numbers based on the time they were discovered through the microscopes on the ship. The average and median radii of spherules discovered later at the Harvard laboratory from the different runs are shown in Table 2.

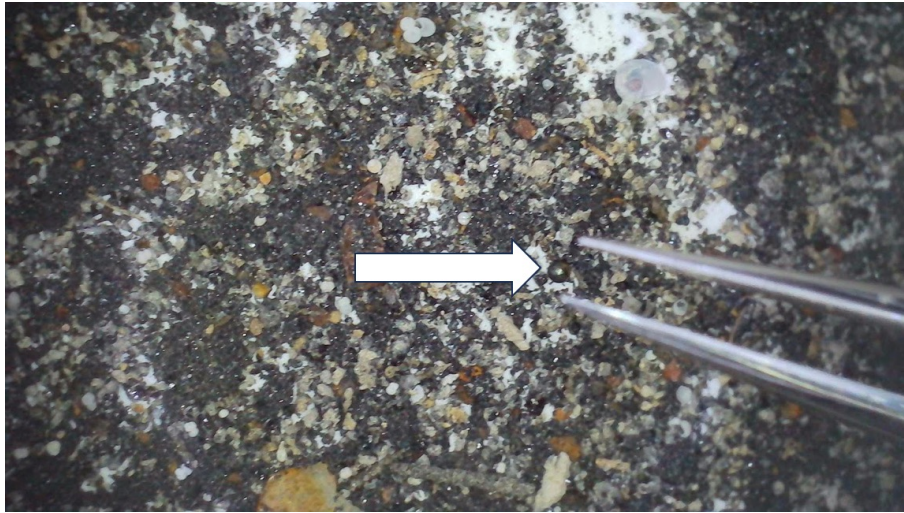


Figure 2. Collected material from the magnetic sled at IM1's site, showing ~ 0.4mm diameter Fe-rich spherule (white arrow) amongst a background of shell hash and other debris

Run	Date (June/2023)	Radius (Microns) per spherule											Count	
1	14	0	0	0	0	0	0	0	0	0	0	0	0	0
2	15	0	0	0	0	0	0	0	0	0	0	0	0	0
3	16	0	0	0	0	0	0	0	0	0	0	0	0	0
4	17	200 (SPH 11)	350 (SPH 12)	200 (SPH 13)	150 (SPH 14)	0	0	0	0	0	0	0	0	4
5	18	75	0	0	0	0	0	0	0	0	0	0	0	1
6	18	150 (SPH 1)	0	0	0	0	0	0	0	0	0	0	0	1
7	19	0	0	0	0	0	0	0	0	0	0	0	0	0
8	20	200 (SPH 4)	150 (SPH 5)	400 (SPH 6)	125 (SPH 7)	200 (SPH 18)	300 (SPH 19)	100 (SPH 20)	150 (SPH 21)	150 (SPH 22)	500 (SPH 23)	200 (SPH 24)	11	11
9	20	400 (SPH 2)	100 (SPH 25)	400 (SPH 28)	0	0	0	0	0	0	0	0	0	3
10	21	0	0	0	0	0	0	0	0	0	0	0	0	0
11	21	0	0	0	0	0	0	0	0	0	0	0	0	0
12	22	150 (SPH 3)	150 (SPH 10)	400 (SPH 26)	0	0	0	0	0	0	0	0	0	3
13	23	550 (SPH 8)	250 (SPH 29)	0	0	0	0	0	0	0	0	0	0	2
14	24	650 (SPH 1)	0	0	0	0	0	0	0	0	0	0	0	1
15	24	110 (SPH 15)	200 (SPH 17)	150 (SPH 30)	0	0	0	0	0	0	0	0	0	3
16	24	400 (SPH 9)	150 (SPH 16)	0	0	0	0	0	0	0	0	0	0	2
17	25	250 (SPH 31)	0	0	0	0	0	0	0	0	0	0	0	1
18	25	0	0	0	0	0	0	0	0	0	0	0	0	0
19	26	180 (SPH 33)	150 (SPH 34)	150 (SPH 35)	210 (SPH 36)	150 (SPH 37)	250 (SPH 38)	200 (SPH 39)	150 (SPH 41)	0	0	0	0	8
20	26	270 (SPH 32)	0	0	0	0	0	0	0	0	0	0	0	1
21	26	200 (SPH 44)	150 (SPH 45)	200 (SPH 46)	130 (SPH 47)	0	0	0	0	0	0	0	0	4
22	26	500 (SPH 40)	110 (SPH 42)	110 (SPH 43)	0	0	0	0	0	0	0	0	0	3
23	27	0	0	0	0	0	0	0	0	0	0	0	0	0
24	27	200 (SPH 48)	150 (SPH 49)	200 (SPH 50)	0	0	0	0	0	0	0	0	0	3

Total spherules: 51

Table 1. Radii of the spherules (in microns) found in different runs on different dates in June 2023 while aboard the M/V Silver Star. Runs 25 and 26 on June 28 were not analyzed because of shortage of time at the end of the expedition.

Run #	# of spherules	Avg. radius (microns)	Median radius (microns)
4	25	168.8	150
5	1	75	75
6	1	150	150
7	2	225	225
8	44	188.2	155
9	17	199.4	150
10	3	150	140
11	26	207.3	170
12	86	169.5	150
13	102	183	160
14	57	194.4	170
15	24	197.9	160
16	23	192.6	170
17	59	314.8	291
18	6	161.7	165
19	43	209.6	180
20	33	191.5	170
21	4	170	175
22	46	220.2	165
23	2	130	130
24	18	201.1	200
Total:	622		

Table 2. Statistical properties of spherules found at Harvard University after the expedition.

5 Spherule Location and Mass Distribution Analysis

The synthetic cable from the ship to the sled was typically ~ 5 km long and the ocean depth is on average ~ 2 km in the search region. Only the vessel GPS coordinates were recorded, not the sled coordinates. Hence, we assign a cross-track error to the ship position to account for the uncertainty on the sled position. Assuming a deviation of the sled track of up to 30 degrees on either side of the ship track, a geometric calculation yields a cross-track error estimate of 2.29 km. We assign to each GPS record a 2.29 km error disc. The union of all discs for a given run constitute the area probed during the run.

The spherule total count n_i for a given run i is weighted by the total mass in grams m_i of magnetic material analyzed from this run, providing the spherule yield parameter, ρ_i :

$$\rho_i = \frac{n_i}{m_i}. \quad (1)$$

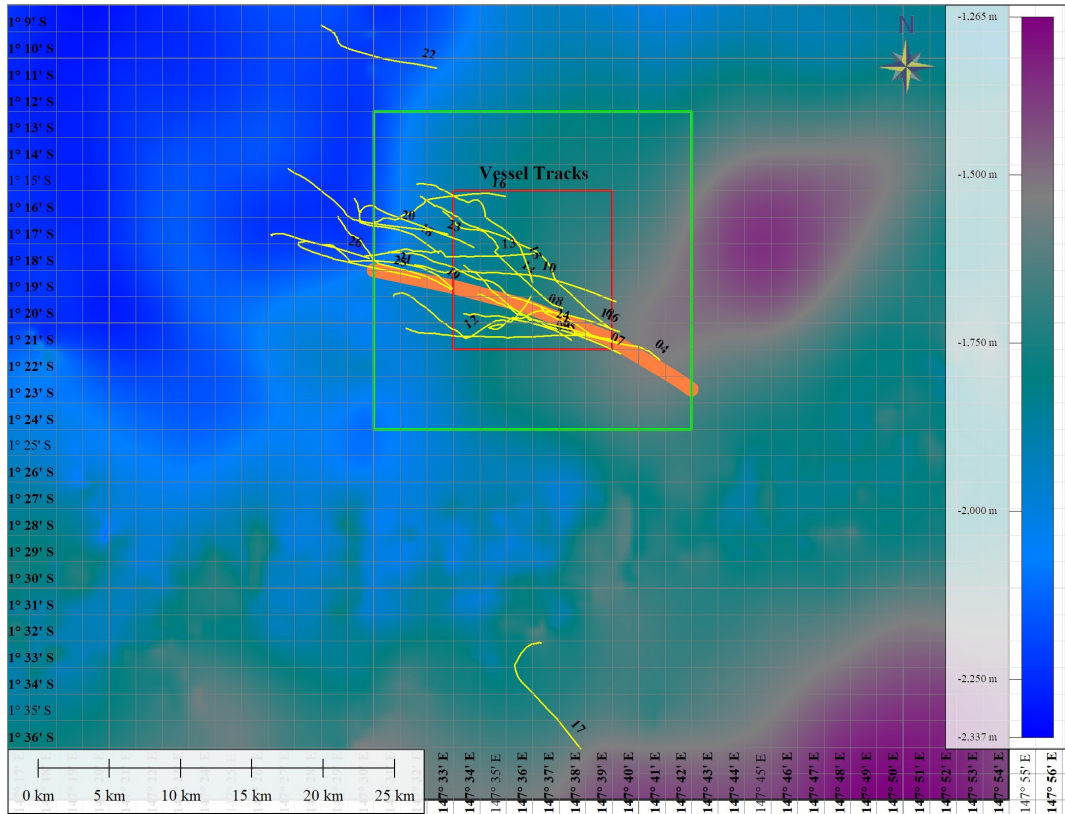


Figure 3. List of ship track numbers around the expected path of IM1 based on seismometer data (Siraj and Loeb, 2023) from Manus Island (orange strip). Background colors indicate ocean depth (with scale on the right). Latitude and longitude are marked in degrees and decimal minutes. At one degree south latitude, one minute of latitude or longitude equals one nautical mile which is 1.852 km. The red box, measuring 11.112 km on a side, marks the uncertainty in the Department of Defence (DoD) localization of IM1’s fireball, and the green box marks twice that size.

Assuming a uniform mass distribution of background magnetic material (mostly volcanic ash) in the sampled area, the amount of magnetic material collected and measured is representative of the total amount of material M_i collected by the sled during run i : $m_i \propto M_i$. Material collected by the sled for a given run can vary due to external factors such as ocean currents, ship speed, sled angle, all of which affect the time spent on the ocean floor. Hence we represent the distribution of spherule counts weighted by the mass of magnetic material analyzed. Spherules were counted in the map only if their diameter was larger than $100 \mu\text{m}$.

We divided the sampled regions into a grid to make a heatmap. The contribution of a run (surface \mathcal{R}_i) to a given square pixel of the map’s grid (surface $\mathcal{A}_{x,y}$) in the heatmap is proportionally weighted by the area overlap of the run and the square. If multiple runs contributed to the same pixel, we assigned the average spherule density to that pixel.

We label as \mathcal{I} the set of run numbers that overlap with a given pixel in row x , column y of the grid. $|\mathcal{I}|$ is the cardinality of this set. The estimated spherule density $\xi_{x,y}$ in this pixel is computed as follows:

$$\xi_{x,y} = \frac{1}{|\mathcal{I}|} \sum_{i \in \mathcal{I}} \frac{|\mathcal{A}_{x,y} \cap \mathcal{R}_i|}{|\mathcal{A}_{x,y}|} \rho_i. \quad (2)$$

Figure 4 shows the resulting heatmap. Each colored pixel is 0.005 degrees (about 0.555 km) on a side. The yellow regions have a spherule density two times larger than the surrounding regions in blue. Figure 5 is a zoomed version of the map onto the region close to the expected path of IM1.

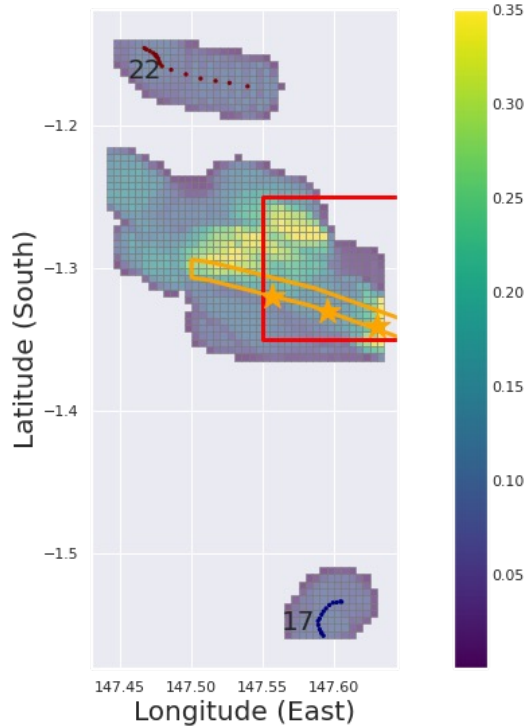


Figure 4. Heatmap of spherule density (count per mass of material analyzed in grams). Assuming that the first flare of the fireball lightcurve was located at the start of run 4, we placed three stars for the locations of the three flares. The color-bar maximum is clipped at 0.35 in this visualization. Each colored pixel in the heatmap is 0.555 km on a side. The negative latitudes stand for southern hemisphere. Runs 22 and 17 (control regions) are also labeled.

The high-yield (yellow) spherule regions occupy less than half of the surveyed area, allowing a fair comparison of the composition of IM1's spherules to background spherules. Given that the highest-yield (yellow) regions in the heat map account for roughly twice the background yield owing to the excess spherules added by IM1, we expect to find a significant numbers of IM1's spherules relative to background spherules in the highest-yield regions. As shown quantitatively in the next section, our composition analysis is consistent with that inference, suggesting that a significant fraction of the spherules in the yellow regions are of interstellar origin.

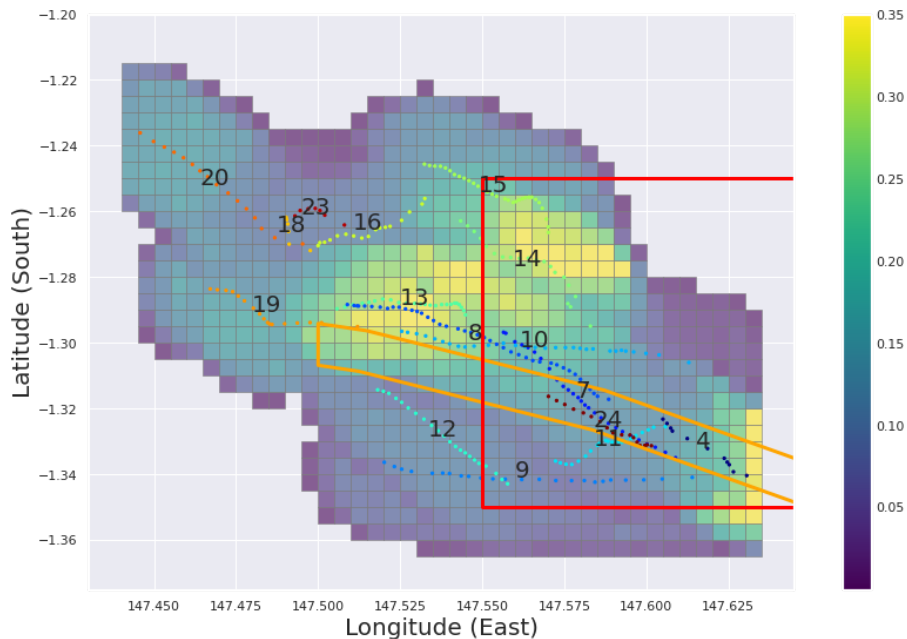


Figure 5. Heatmap of spherule density (count per mass of material analyzed in grams), zoomed onto the region sampled around the predicted IM1 path (orange box) and the DoD error region (red box). For reference, the dots represent the GPS recordings of the ship track in different numbered runs. The color-bar maximum is clipped at 0.35 in this visualization. Each pixel in this heatmap is 0.555 km on a side.

6 Spherule Samples and Location

The retrieval of cosmic spherules from meteor sites has a long history, with related morphology and composition analyses linking them to various components of the solar system (Brownlee et al., 1979; Maurette et al., 1991; Taylor and Brownlee, 1991; Xue et al., 1994; Brownlee et al., 1997; Herzog et al., 1999; Taylor et al., 2000; Engrand et al., 2005; Genge et al., 2008; Vondrak et al., 2008; Wittke et al., 2013; Folco et al., 2015; Rudraswami et al., 2015; Genge et al., 2017).

As demonstrated by the composition analysis described in the upcoming subsections, the excess ablation spherules collected from IM1's path are substantially different from the spherules collected in our control areas, which are expected to be solar system materials.

Table 3 shows the samples selected for elemental and isotopic measurements. The selected spherules range in diameter from 0.25 to 1.7 mm. They have been classified as I, S and D-types including some subclasses based on our measurements of their chemical compositions. The terminology and measurements will be explained in the upcoming subsections. We selected a substantial number of spherules from runs 4, 8, 13 and 14 along IM1's path in Fig. 5. Additional spherules were selected from run 22 and run 17, as they are not on IM1's path and provide the background abundance patterns for spherules from the solar system.

Table 3: Spherules analyzed for major and trace elements

Vial top label	Spherule name	Run #	Type	Subclass	Calculated mass (mg)	Diameter (mm)
S10	IS4B SPH1	4	D-Type	BeLaU	0.327	0.500
S21	IS14 SPH1	14	D-Type	BeLaU	1.727	0.871
no label	(6) IS14 SPH4	14	D-Type	BeLaU	9.218	1.522
no label	(19) IS4 SPH8	4	D-Type	BeLaU	0.847	0.687
no label	(25) IS13 SPH5	13	D-Type	BeLaU	2.087	1.045
no label	IS14 SPH2	14	D-Type	Low-La	2.681	1.008
no label	IS14 SPH3	14	D-Type	Low-La	0.209	0.431
no label	IS17 SPH1	17	D-Type	Low-La	0.096	0.332
no label	(1) IS22 SPH1	22	D-Type	Low-La	9.979	1.760
no label	(3) IS13 SPH8	13	D-Type	Low-La	1.579	0.845
no label	(11) IS14 SPH11	14	D-Type	Low-La	0.250	0.457
no label	(13) IS17 SPH3	17	D-Type	Low-La	0.270	0.528
no label	(14) IS17 SPH4	17	D-Type	Low-La	0.583	0.683
no label	(15) IS17 SPH5	17	D-Type	Low-La	0.383	0.593
no label	(17) IS4 SPH6	4	D-Type	Low-La	1.151	0.761
no label	(18) IS4 SPH7	4	D-Type	Low-La	0.575	0.604
no label	(21) IS8 SPH3	8	D-Type	Low-La	0.822	0.680
no label	(28) IS13 SPH8b	13	D-Type	Low-La	4.058	1.304
no label	(30) IS13 SPH12	13	D-Type	Low-La	1.982	0.912
no label	(31) IS14 SPH5	14	D-Type	Low-La	1.688	0.864
no label	(32) IS14 SPH6	14	D-Type	Low-La	0.425	0.546
no label	IS13 SPH3	13	I-type	Ni-rich	0.146	0.383
S11	IS4C SPH2	4	I-type	Ni-rich	0.097	0.333
no label	(12) IS14 SPH14	14	I-type	Ni-rich	0.496	0.575
no label	(24) IS8 SPH6	8	I-type	Ni-rich	0.832	0.682
S16	IS12C SPH1	12	I-type	Ni, Mn-poor	0.902	0.701
no label	IS8 SPH1	8	I-type	Ni-poor	0.497	0.575
no label	IS8 SPH2	8	I-type	Ni-poor	0.117	0.355
S7	IS16A SPH1	16	I-type	Ni-poor	0.836	0.684
S23	IS19 SPH1	19	I-type	Ni-poor	0.116	0.354
S29	IS19 SPH7	19	I-type	Ni-poor	0.157	0.392
S31	IS19 SPH8	19	I-type	Ni-poor	0.119	0.357

Vial top label	Spherule name	Run #	Type	Subclass	Calculated mass (mg)	Diameter (mm)
S5	IS8-SPHR	8	I-type	Ni-poor	0.246	0.455
S19	IS13B SPH2	13	I-type	Ni-poor	0.495	0.574
no label	(2) IS22 SPH4	22	I-type	Ni-poor	4.643	1.211
no label	(5) IS13 SPH9	13	I-type	Ni-poor	2.840	1.028
no label	(10) IS14 SPH10	14	I-type	Ni-poor	0.777	0.667
no label	(22) IS8 SPH4	8	I-type	Ni-poor	0.615	0.617
no label	(26) IS13 SPH6	13	I-type	Ni-poor	2.068	0.925
no label	IS4 SPH4	4	S-type	Chondritic	0.149	0.434
no label	IS4 SPH5	4	S-type	Chondritic	0.071	0.338
no label	IS13 SPH4	13	S-type	Chondritic	0.122	0.405
no label	IS17 SPH2	17	S-type	Chondritic	0.075	0.345
S25	IS19 SPH2	19	S-type	Chondritic	0.079	0.351
S12	IS4D SPH3	4	S-type	Chondritic	0.078	0.349
S9	IS4A SPHS	4	S-type	Chondritic	0.156	0.440
no label	IS22 SPH2	22	S-type	Chondritic	0.027	0.244
no label	IS22 SPH3	22	S-type	Chondritic	0.029	0.251
no label	(4) IS13 SPH11	13	S-type	Chondritic	0.639	0.704
no label	(7) IS14 SPH7	14	S-type	Chondritic	2.793	1.151
no label	(8) IS14 SPH8	14	S-type	Chondritic	0.711	0.730
no label	(9) IS14 SPH9	14	S-type	Chondritic	0.737	0.738
no label	(16) IS22 SPH5	22	S-type	Chondritic	1.793	0.993
no label	(20) IS4 SPH9	4	S-type	Chondritic	0.391	0.598
no label	(23) IS8 SPH5	8	S-type	Chondritic	0.597	0.688
no label	(27) IS13 SPH7	13	S-type	Chondritic	0.806	0.761
no label	(29) IS13 SPH10	13	S-type	Chondritic	0.658	0.711

7 Analytical Methods

We studied the spherules in four laboratories at Harvard University, UC Berkeley, Bruker Corporation in Germany and the University of Technology in Papua New Guinea. The elemental and isotopic measurements reported here are primarily from the Harvard Laboratory ⁴. Additional results are mentioned in Appendix C and more will be presented in future publications.

⁴<https://projects.iq.harvard.edu/geochemistry>

7.1 Electron microprobe analysis

Major element spot analyses and imaging of the spherules were performed with the JEOL Model JXA 8230 Electron Probe Microanalyzer (EPMA) in the Cosmochemistry Laboratory at Harvard University. The instrument uses either tungsten pin or LaB₆ filaments to generate an electron beam. The instrument is a high resolution, highly stable scanning electron microscope (SEM) equipped with 4 wavelength-dispersive spectrometers (WD) and one dry energy-dispersive (ED) spectrometer. The combination of 4 wavelength dispersive X-ray spectrometers (WDS) and a JED-2300 dry energy dispersive X-ray spectrometer (EDS) can simultaneously analyze 4 elements by WDS and many elements by EDS. This enables for example major elements measurements by EDS, and trace elements by WDS to save time. The operation software allows simultaneous displaying of up to 4 images including a backscattered electron image (BEI), a secondary electron image (SEI), a cathode-luminescence image (CLI), and X-ray images. In addition to point, line and area analysis and BSE, SEI, CLI, and X-ray imaging, the EPMA is capable for acquiring detailed chemical maps of larger areas which can be converted to phase or concentration maps using the built-in software and exported as images or digital maps for an off-line processing. Some samples are mounted in epoxy while others are on carbon tape for the imaging and spot measurements of the spherules.

7.2 Triple Quad elemental analysis

Measurements of elemental abundances for major and trace elements were performed on the iCAP TQ quadrupole ICP-MS (ThermoFisher Scientific) in the Cosmochemistry Laboratory at Harvard University. USGS reference materials were thoroughly dissolved and diluted in a 2% HNO₃ solution spiked with 2 ppb indium diluted to a factor of 5000 to be used as standards. Spherules were prepared for mass spectrometry measurements by first individually digesting the samples in a mixture of concentrated HF-HNO₃-HCl at a 1:3:1 ratio at 120-140°C overnight. The samples were subsequently dried down and then redissolved in a second acid mixture involving an aqua regia solution mixed with H₂O at a 3:2 ratio and heated to 120°C overnight. This dissolution was dried down for the second time and redissolved in a high-purity 2% HNO₃ solution. A small aliquot (3%) was drawn from this solution and further diluted for elemental analysis. To account for and to correct instrumental drift, the 2% HNO₃ solution used for dilution was spiked with 2 ppb indium as an internal standard, prepared identically to the standard solutions. Measurements were performed in KED mode with He as a collision cell gas as recommended by the Reaction Finder function built in the iCAP TQ software, with the exception of Cr, which was measured in TQ mode with O₂ as a mass-shifted molecule. The prepared spherule solutions were measured as an unknown against a four-point calibration line consisting of a blank and three USGS standards: BCR-2 BHVO-2, and AGV-2. Calibration curves for individual elements were checked for linear intensity to concentration correlations for accurate measurements. Routine measurements of AGV-2 as an unknown on the iCAP TQ suggest fractional errors to be within 6% using this method.

7.3 Iron isotope analysis with the Collision Cell Multicollector ICP

Measurements of iron isotopes were performed with the Nu Sapphire multi-collector inductively coupled plasma mass spectrometer (MC-ICPMS) in the Cosmochemistry Laboratory at Harvard University. All Fe ion beams may be affected by molec-

ular interferences from argide ions. Hydrogen and He were introduced into the collision-reaction cell of the instrument to reduce interferences from Ar-related species ($^{40}\text{Ar}^{14}\text{N}^+$ on ^{54}Fe , $^{40}\text{Ar}^{16}\text{O}^+$ on ^{56}Fe and $^{40}\text{Ar}^{16}\text{O}^1\text{H}^+$ on ^{57}Fe). Sample solutions were introduced into the instrument using an Elemental Scientific Apex Omega desolvating spray chamber with a 100 microliter per minute PFA nebulizer. Iron was purified from the sample matrix by passing an aliquot of solution once through BioRad AG1-X8 ion-exchange resin. Solution Fe purity was checked by Quadrupole MC-ICPMS, prior to isotopic analysis. Iron isotope ratios ($^{56}\text{Fe}/^{54}\text{Fe}$, $^{57}\text{Fe}/^{54}\text{Fe}$) were analyzed by sample-standard bracketing relative to a lab standard. Sample and standard solutions were prepared at concentrations of about 70 ppb. All solutions were matched in concentration to within about 2% or better to avoid significant concentration-related matrix effects.

Mass-dependent isotope values are reported as δ -values. The $\delta^{56/54}\text{Fe}$ and $\delta^{57/54}\text{Fe}$ values are defined as the per mil deviations of the measured isotope ratios, $(^{56}\text{Fe}/^{54}\text{Fe})_{\text{meas}}$ and $(^{57}\text{Fe}/^{54}\text{Fe})_{\text{meas}}$, relative to the same ratios in a standard (std):

$$\delta^{56/54}\text{Fe} = \left(\frac{\left(\frac{^{56}\text{Fe}}{^{54}\text{Fe}} \right)_{\text{meas}}}{\left(\frac{^{56}\text{Fe}}{^{54}\text{Fe}} \right)_{\text{std}}} - 1 \right) \times 10^3, \quad (3)$$

$$\delta^{57/54}\text{Fe} = \left(\frac{\left(\frac{^{57}\text{Fe}}{^{54}\text{Fe}} \right)_{\text{meas}}}{\left(\frac{^{57}\text{Fe}}{^{54}\text{Fe}} \right)_{\text{std}}} - 1 \right) \times 10^3. \quad (4)$$

Analyses of the common standard NIST IRMM-14 were obtained relative to the lab standard, so that δ -values relative to the lab standard can be easily converted and compared to literature values for iron isotopes relative to NIST IRMM-14.

In addition, the $^{57}\text{Fe}/^{54}\text{Fe}$ ratio was corrected for mass fractionation using the $^{56}\text{Fe}/^{54}\text{Fe}$ ratio. The $\varepsilon^{57/54}\text{Fe}$, defined as the part in 10^4 deviation of the fractionation corrected isotope ratios, $\left(\frac{^{57}\text{Fe}}{^{54}\text{Fe}} \right)_{\text{meas}(N)}$, relative to the same ratio in a standard (std), is:

$$\varepsilon^{57/54}\text{Fe} = \left(\frac{\left(\frac{^{57}\text{Fe}}{^{54}\text{Fe}} \right)_{\text{meas}(N)}}{\left(\frac{^{57}\text{Fe}}{^{54}\text{Fe}} \right)_{\text{std}}} - 1 \right) \times 10^4, \quad (5)$$

Uncertainties reported in figures and tables are internal mass spectrometric errors, and the true uncertainties may be somewhat greater.

7.4 Imaging, morphology and chemical spot analyses of the spherules

Spherules collected near IM1's path appear to be nested (see Appendix C), suggesting that liquid drops engulfed smaller ones which solidified earlier. The dendritic textures of these spherules suggests rapid cooling.

Figure 6 shows an electron microprobe image of a modest-size (0.7 mm in diameter) spherule IS16A SPH1 from run 16. An example of a large (1.3 mm in maximum diameter, 0.9 mm average) spherule in the high-yield (yellow) region along IM1's path is S21 (IS14-SPH1) from run 14. This lopsided spherule, shown in Figure 7, is a composite of three spherules that solidified

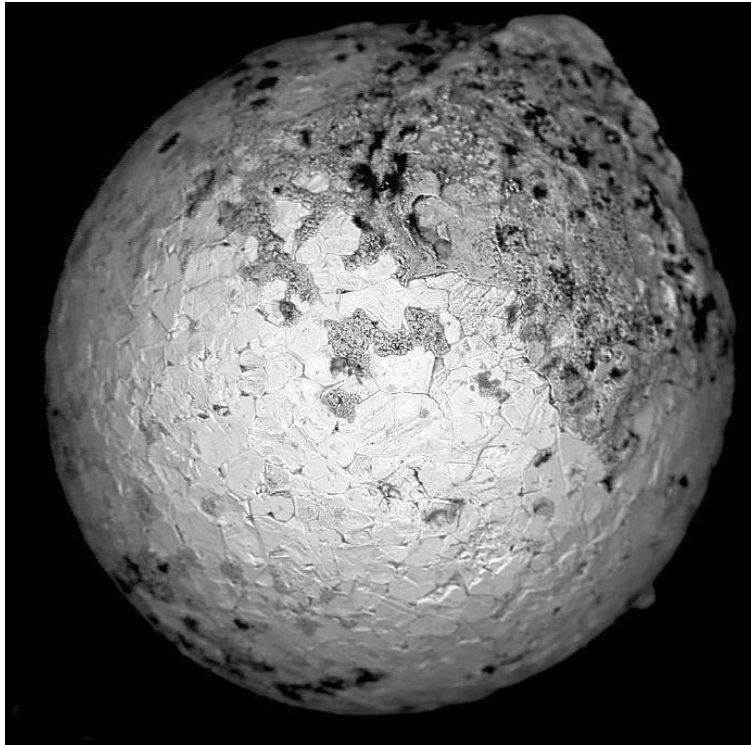


Figure 6. Electron microprobe image of spherule IS16A SPH1 from run 16.

shortly after merger but too late for the merger product to become spherical. The mass of S21 (1.7 mg) is about twice that of IS16A SPH1 (0.84 mg).

The existence of a triple-merger like S21 can be explained as a product of IM1's airburst. The total mass collected by spherules in our 26 runs is of order $\sim 1\text{g}$. Given the sled's width of 1m, the total surveyed area, $\sim 0.26\text{ km}^2$, constitutes a fraction of $\sim 10^{-2}$ of IM1's strewn field, defined by the yellow regions in Figure 5. This implies a total mass in IM1's spherules of order $\sim 100\text{g}$, as expected given that most of IM1's mass evaporated to undetectable particles (well below tens of μm in size) or gas (Tillinghast-Raby et al., 2022). Assigning a mass of $\sim 10^{-3}\text{g}$ per spherule implies a total number of $\sim 10^5$ such spherules. Based on IM1's speed and fireball energy, the total mass ablated by IM1's fireball is $\sim 5 \times 10^5\text{g}$ corresponding to an object radius of $R \sim 50\text{cm}$ (Siraj and Loeb, 2022a). The total number of spherules divided by the initial volume associated with R yields an initial spherule number density of $n \sim 0.2\text{ cm}^{-3}$ which gets diluted considerably as the material expands. For the characteristic diameter of a spherule, $\sim 1\text{mm}$, the geometric cross-section for spherule-spherule collisions is $\sigma \sim 3 \times 10^{-2}\text{ cm}^2$. The resulting collision probability is $\tau \sim n\sigma R \sim (0.2\text{ cm}^{-3}) \times (3 \times 10^{-2}\text{ cm}^2) \times (50\text{ cm}) \sim 0.3$, implying a likelihood of $\tau^2 \sim 0.1$ for triple-spherule mergers such as S21. Mergers that occur inside a liquid envelope would result in a spherical shell with embedded sub-spherules inside of it, as shown in the images of Appendix C.

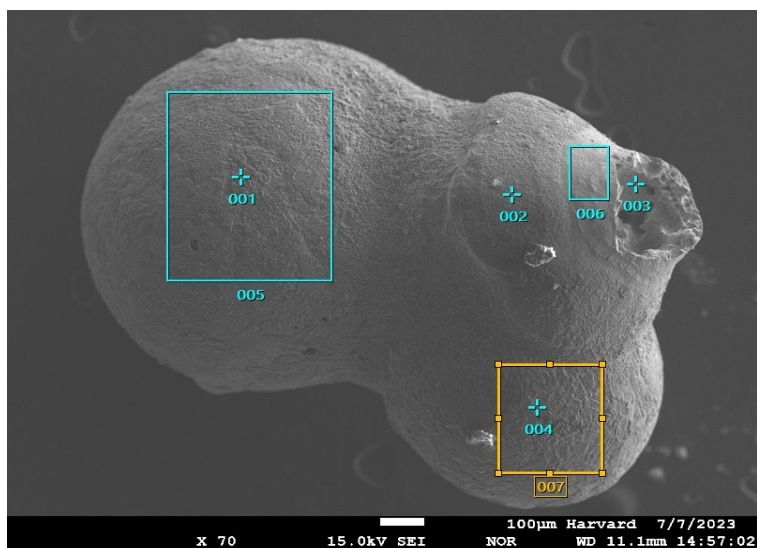


Figure 7. Electron microprobe image of the spherule S21 (IS14-SPH1) from run 14 in the high yield region of IM1's path. The elemental abundances measured in different regions on the surface are displayed in Table 4.

Element	Pt#1 (weight %)	Pt#2 (weight %)	Pt#3 (weight %)	Pt#4 (weight %)	Pt#5 (weight %)	Pt#6 (weight %)	Pt#7 (weight %)
C	0.64		0.7	1.5	2.1	5.48	2.66
O	13.95	28.9		32.35	29.18	18.66	34.19
Na	0.63	0.73			0.7	0.72	
Mg	0.28				0.42	0.15	
Al	2.93	3.48		1.15	2.45	1.44	1.18
Si	6.4	10.85			2.92	4.2	0.97
P		0.31					
Cl	0.26	0.4			0.51	1.28	
K	0.39						
Ca	3.88	4.55			1.73	1.85	0.23
Cr					0.31		
Fe	70.65	50.78	99.3	65.01	59.69	66.22	60.77
Total	100	100	100	100	100	100	100

Table 4. Electron microprobe data on the chemical composition in the different regions on the surface of S21, as labeled in Figure 7.

7.5 Classification by elemental composition measurements of bulk spherules

We used Figure 8 and tables 2 and 3 in a review by Folco et al. (2015) to classify the 57 spherules listed in Table 4. Our elemental data are provided in Appendix A. The elements are plotted as a function of their volatility in Figures 8, 9 and 10, using the same elements as Folco et al. (2015) in their Figure 8. This resulted in 18 spherules being classified as standard S-type chondritic spherules (Figure 8) and another 18 spherules being classified as standard I-type spherules (Figure 9). Four of the I-type spherules are Ni-rich, while the rest are Ni-poor. In addition, we identified 21 spherules that are clearly derived from material that has gone through planetary differentiation as they have many features, such as low Mg, that are typical of planetary differentiation (Figure 10). They are all different from the differentiated spherule pattern described by Folco et al. (2015). We refer to these new types of differentiated spherules as D-type spherules. These have never been described in the cosmic spherule literature. There are two subtypes of the D-type differentiated spherules. We call the subtypes Low-La and “BeLaU” and their distinct elemental patterns are shown in Figure 10. The “BeLaU” spherules have refractory lithophile element abundances that are 80 to 1,000 higher than in CI chondrites. The highly enriched “BeLaU” spherules (enriched in Be, La, U and many other refractory lithophile elements) will be discussed in more detail in the next section. Figure 11 shows the CI-normalized Mg and La for the 57 spherules. These two elements provide a relatively clear distinction between the spherule groups discussed here.

A summary of spherule types found in individual runs is listed in Table 5. This shows that “BeLaU”-type spherules are only found in runs 4, 13 and 14 which overlap with the high yield (yellow) IM1 regions in the heatmap of Fig. 5. The lines of these three runs also stretch across low-yield regions which moderate their average yield of “BeLaU” spherules. With less than a third of the total length of runs 4, 13 and 14 lying in high-yield (yellow) regions, the retrieval of 5 “BeLaU”-type spherules out of a total of 34 spherules analyzed in these three runs, suggests that the high-yield (yellow) regions should have comparable numbers of “BeLaU”-type and background spherules. This agrees with the enhancement by a factor of ~ 2 in the number of spherules per unit mass associated with the high-yield (yellow) regions along IM1’s path, compared to the background (green-purple) in the heatmap of Fig. 5.

7.6 Significance of the novel “BeLaU”-type spherules

The spherules with enrichment of beryllium (Be), lanthanum (La) and uranium (U), labeled “BeLaU”, appear to have an exotic composition different from other solar system materials. The results for the “BeLaU” spherule S21 are displayed in Figures 12, 13 and 14. We use this spherule to point out some of the unique feature of the “BeLaU” elemental composition.

A plot of the elemental abundances of the spherule S21 (normalized to CI chondrites) as a function of atomic number for 56 elements is shown in Figure 12. Across the diagram the peak abundances are for Be, La and U, hence the name “BeLaU”. The abundance pattern of S21 implies derivation from a planetary crust, highly enriched in refractory lithophile elements (red dots). The volatile element abundances (green dots) are very low, suggesting either derivation from an extremely volatile-depleted planet or evaporative loss during passage through the Earth’s atmosphere. The very low content of refractory siderophile elements with affinity to iron (Re) suggest a source planet with an Fe core. A plot of the abundance pattern of elements in spherule S21 as a function of the volatility sequence used by Folco et al. (2015) is shown in Figure 13. Since there are strong

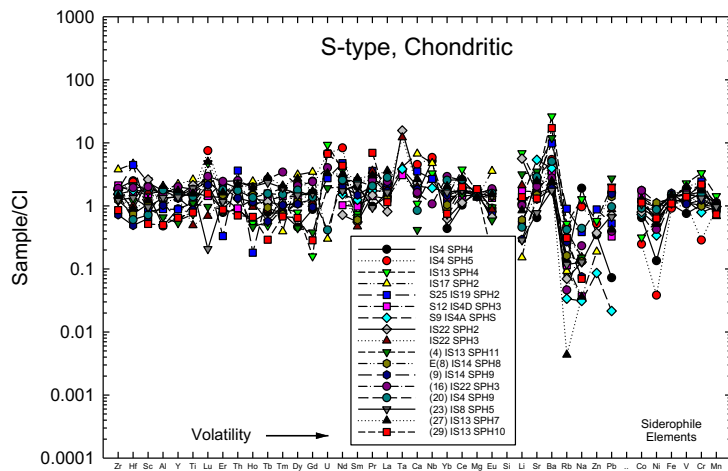


Figure 8. Abundances of elements as a function of their volatility for S-type chondritic spherules from run 4, 8, 9, 12, 13, 14, 17, 19 and 22.

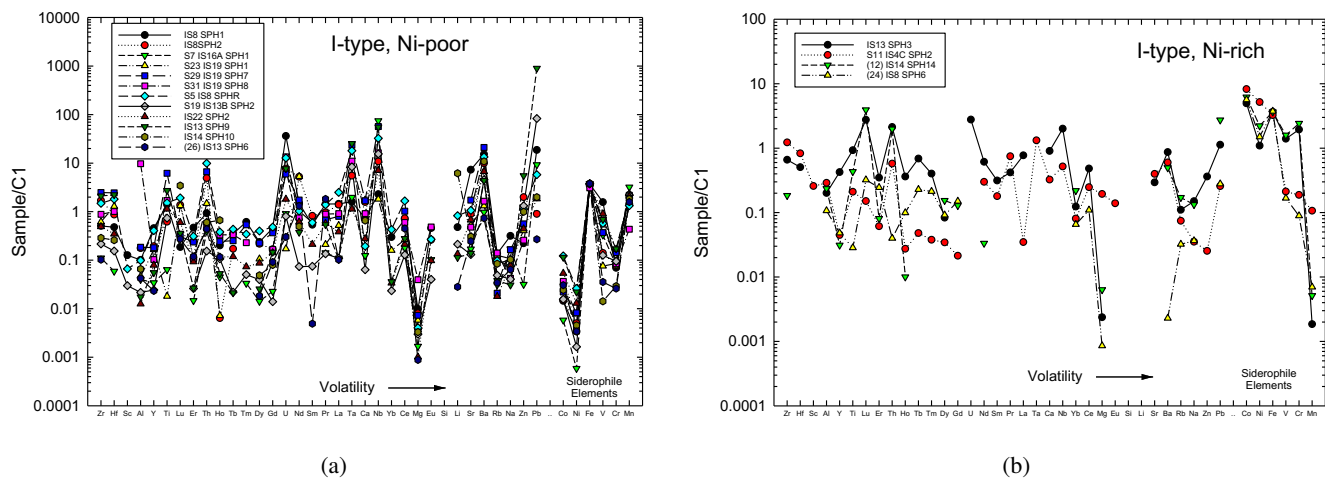
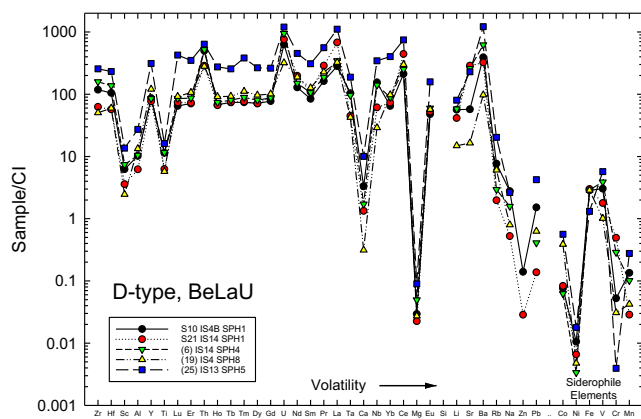
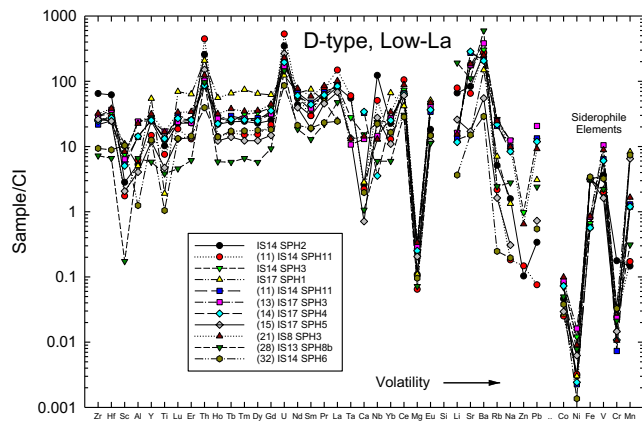


Figure 9. Abundances of elements as function of their volatility in I-type spherules. (a) I-type, Ni-poor spherules from runs 8, 13, 14, 16, 19, and 22. (b) I-type, Ni-rich spherules from runs 4, 8, 13 and 14.



(a)



(b)

Figure 10. Abundances of elements as function of their volatility for D-type spherules: (a) “BeLaU”-type spherules from runs 4, 13 and 14, from the high-yield regions near IM1’s path; and (b) D-type, Low-La spherules from runs 8, 13, 14 and 17.

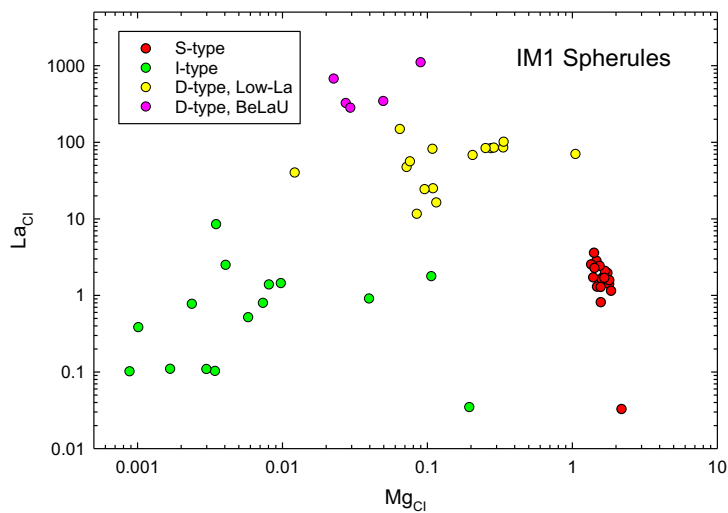


Figure 11. CI-normalized Mg and La for the 57 analyzed spherules.

Run	Number of spherules	S-type	I-type	D-type (Low-La)	D-type (BeLaU)
IS4	10	5	1	2	2
IS8	7	1	5	1	0
IS12	1	0	1	0	0
IS13	12	4	4	3	1
IS14	12	3	2	5	2
IS16	1	0	1	0	0
IS17	5	1	0	4	0
IS19	4	1	3	0	0
IS22	5	3	1	1	0
Total	57	18	18	16	5

Table 5. Results summary for 57 spherules analyzed for major and trace element composition.

indications that the spherules are derived from a differentiated planet, the data are also plotted in Figure 14 as a function of an igneous compatibility sequence. Compatibility is a geochemical parameter measuring how readily a particular element substitutes for a major element in mantle source minerals during melting to produce magma. It also roughly represents the sequence of enrichments of elements in a crystallizing magma.

The abundances of elements as function of their compatibility for all 5 “BeLaU”-type spherules are shown in Figure 15. They are all from runs 4, 13 and 14, the high-yield (yellow) regions near IM1’s path. The “BeLaU” spherules’ variations in the abundances of trace elements relative to CI chondrites are higher by 1-3 orders of magnitude compared to cosmic spherules from the solar system reviewed by Folco et al. (2015). This “BeLaU” abundance pattern found in IM1’s spherules could have possibly originated from a highly differentiated planetary magma ocean.

The “BeLaU” element patterns are compared in Figure 16 with the highly enriched sources of differentiated bodies in the solar system, including Earth’s upper continental crust (Rudnick and Gao, 2014) and kimberlites (Giuliani et al., 2020), lunar magma ocean residual liquid (KREEP) (Warren, 1989), Shergottites from Mars (Lodders, 1998; Jambon et al., 2002) and eucrites from Vesta (Kitts and Lodders, 1998). Figure 16 presents the comparison of refractory lithophiles that are not easily lost by evaporation or altered by fluids. Shergottites and eucrites are markedly distinct from the “BeLaU” samples due to the systematically lower incompatible element enrichments. The upper continental crust is also overall depleted in incompatible elements compared to “BeLaU”. Additionally, “BeLaU” samples have prominent negative anomalies of Ti, Li, higher Lu/Al, and variable Be and Sr enrichments that do not match the smooth pattern of the upper continental crust. Kimberlite is also remarkably distinguished from the “BeLaU” pattern in their Ta and Nb positive anomalies and the strong heavy rare earth element depletion. Lastly, despite the resembling overall element enrichments, the lunar KREEP displays pronounced differences in light rare earth element enrichment and strong Sr, Eu, and Cr negative anomalies from “BeLaU” that distinguish the two

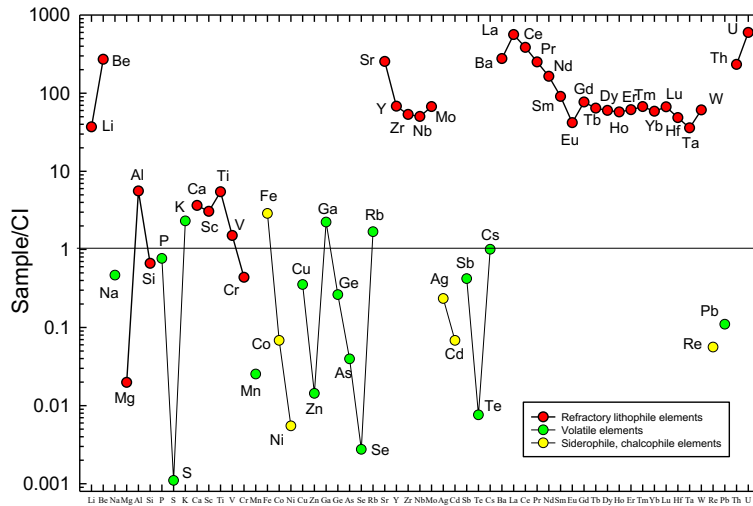


Figure 12. The “BeLaU” elemental abundances of the spherule S21 (normalized to CI chondrites) versus atomic number for 56 elements. The solar system standard of CI chondrites is represented by a value of unity on the plot.

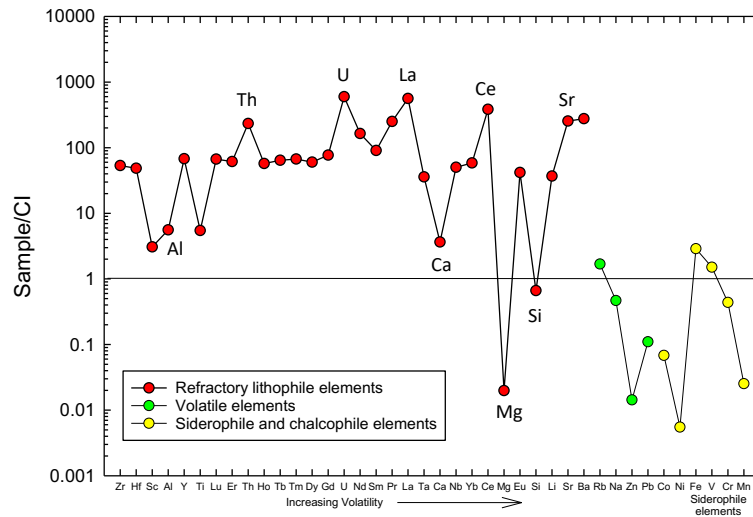


Figure 13. The abundance pattern of elements in spherule S21 versus volatility.

groups. We conclude that the “BeLaU” samples possibly reflect an extremely evolved composition from a planetary magma ocean, but not the known bodies within the solar system.

Table 3 shows that “BeLaU”-type spherules were retrieved from runs 4, 13 and 14 in the high-yield (yellow) regions near IM1’s path in Fig. 5. Additional spherules from run 22 and run 17 in control regions exhibited background abundance patterns from the solar system.

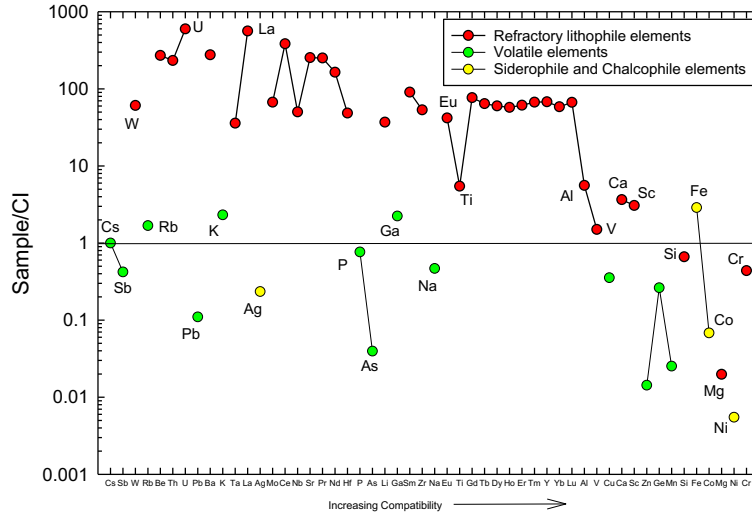


Figure 14. Abundances versus compatibility (see text) for S21. Elements ordered with increasing compatibility towards the right.

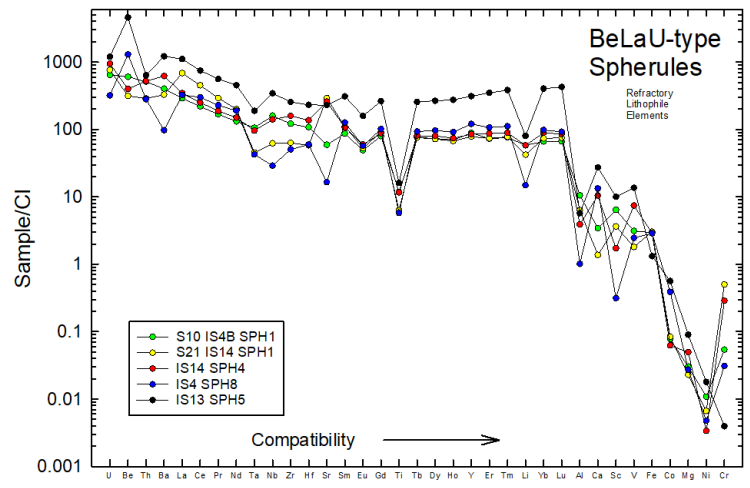


Figure 15. Abundances of elements as function of their compatibility for all “BeLaU”-type spherules. They are all from runs 4, 13 and 14, the high-yield (yellow) regions near IM1’s path in Fig. 5.

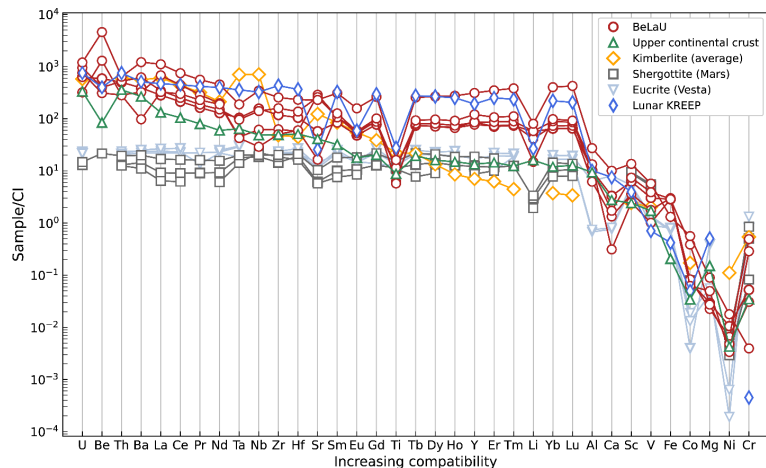


Figure 16. The “BeLaU” element abundance pattern has features that make it distinct from enriched sources on solar system bodies. Elements are ordered with increasing compatibility. Data source: Earth’s upper continental crust (Rudnick and Gao, 2014); kimberlites (Giuliani et al., 2020); lunar KREEP (Warren, 1989); shergottites [Shergotty, Zagami, and Los Angeles meteorites] (Lodders, 1998; Jambon et al., 2002); eucrites [Bouvante, Pomozdino, and Stannern meteorites] (Kitts and Lodders, 1998).

7.7 Iron isotope measurements of the spherules

The iron isotope data for the selected spherules are reported in Table 6 as $\delta^{56/54}\text{Fe}$ and $\delta^{57/54}\text{Fe}$ values relative to our lab standard. We also report fractionation corrected $^{57}\text{Fe}/^{54}\text{Fe}$ ratios as $\epsilon^{57/54}\text{Fe}$ values. We measured 9 spherules for iron isotopes, 7 of them from close to IM1’s path and 2 from a distant region (run 22). The $\delta^{56/54}\text{Fe}$ and $\delta^{57/54}\text{Fe}$ results are shown in Figure 17. Note that the δ -scales are relative to our Fe isotope lab standard and not IRMM-14, which has $\delta^{56/54}\text{Fe} = 0.207$ relative to our lab standard. Figure 17 also shows the calculated trend for mass-dependent fractionation following the exponential fractionation law of Russell et al. (1978). We also measured a hydrothermal terrestrial magnetite (OR-13) from a bismuth ore deposit associated with the Drammen Granite in Viken, Norway. The OR-13 magnetite has a $\delta^{56/54}\text{Fe}$ value of -0.141 and was used together with IRMM-14 to test and monitor the methods for Fe isotope measurements. All measurements fall along the mass-dependent curve.

The mass-dependent Fe isotope effects of the spherules are well resolved and generally much larger than for typical Solar System planetary reservoir values. They are outside the range of typical values for planetary basalts from Mars, Earth, Moon, Vesta, the parent bodies of Angrites and Ureilites (Sossi et al., 2016; Ni et al., 2020) and the upper continental crust estimate is from (Gong et al., 2017). The only solar system materials with clearly larger fractionations are the I-type cosmic spherules (Engrand et al., 2005). Engrand et al. (2005) found large, correlated, mass-dependent enrichments in the heavier isotopes of O, Cr, Fe, and Ni in I-type cosmic spherules collected from the deep sea, with $\delta^{56/54}\text{Fe}$ in the range +20 to +36. They concluded that the isotopic fractionation and the I-type spherules are consistent with a Rayleigh distillation of the molten objects as they evaporate during their passage through the Earth’s atmosphere. Since the range in $\delta^{56/54}\text{Fe}$ for S-type spherules

Spherule type	Vial top label	Spherule name	$\delta^{56/54}\text{Fe}$	$\pm 1\sigma$	$\delta^{57/54}\text{Fe}$	$\pm 1\sigma$	$\epsilon^{57/54}\text{Fe}$	$\pm 1\sigma$
BeLaU spherules								
BeLaU	S10	IS4B-SPH1	-0.2	0.002	-0.335	0.011	-0.18	0.14
BeLaU	S21	IS14-SPH1	1.073	0.010	1.581	0.061	-0.25	0.44
BeLaU	S21-repeat	IS14-SPH1	1.054	0.004	1.516	0.083	-0.4	0.89
I-type spherules (Ni-rich)								
I-type	S11	IS4C-SPH2	2.668	0.012	3.911	0.042	-0.6	0.51
I-type spherules (Ni-poor)								
I-type	S5	IS8-SPHR	-0.663	0.016	-0.962	0.035	0.04	0.54
I-type	S19	IS13B-SPH2	-0.488	0.029	-0.847	0.053	-1.2	0.24
S-type spherules								
S-type	S9	IS4A-SPHS	2.138	0.014	3.083	0.103	-0.99	0.92
S-type	S12	IS4D-SPH3	0.571	0.005	0.794	0.050	-0.55	0.45
S-type	No label	IS22-SPH2	2.246	0.004	3.142	0.045	-2.00	0.45
S-type	No label	IS22-SPH3	1.712	0.115	2.524	0.097	-0.23	1.32
IRMM-14 standard and terrestrial magnetite sample								
IRMM-14	No label	standard	0.207	0.009	0.266	0.044	-0.38	0.63
OR-13	No label	magnetite	-0.141	0.008	-0.237	0.03	-0.16	0.27

Table 6. Iron isotope measurements for different spherule types.

were smaller (+1.4 to 3.2), Engrand et al. (2005) concluded that mass losses due to evaporation were probably small for most S-type spherules. The range of observed iron isotope fractionation in the IM1 "BeLaU"-type spherules ($\delta^{56/54}\text{Fe}$ in the range -0.7 to + 2.7) is smaller than for typical I-type spherules in the Engrand et al. (2005) study and similar to their two S-type spherules. This suggests evaporation from IM1 during an airburst in the lower atmosphere of the Earth, which would suppress the magnitude Rayleigh isotope distillation effects in these spherules.

The measured $\epsilon^{57/54}\text{Fe}$ values are mostly within error of the terrestrial value. Small effects could be present, but this needs to be further investigated with more precise measurements and including $\epsilon^{58/54}\text{Fe}$ measurements. There are no well resolved nucleosynthetic variations ($\epsilon^{57/54}\text{Fe}$ values) at the level of precision obtained.

8 Conclusions

The magnetic sled survey around IM1's path during the period of 14-28 June, 2023 discovered about 700 spherules of diameter 0.05-1.3 millimeters through 26 runs surveying 0.26 km². The spatial distribution of these spherules is significantly concentrated along the bolide path, as shown in Figure 4.

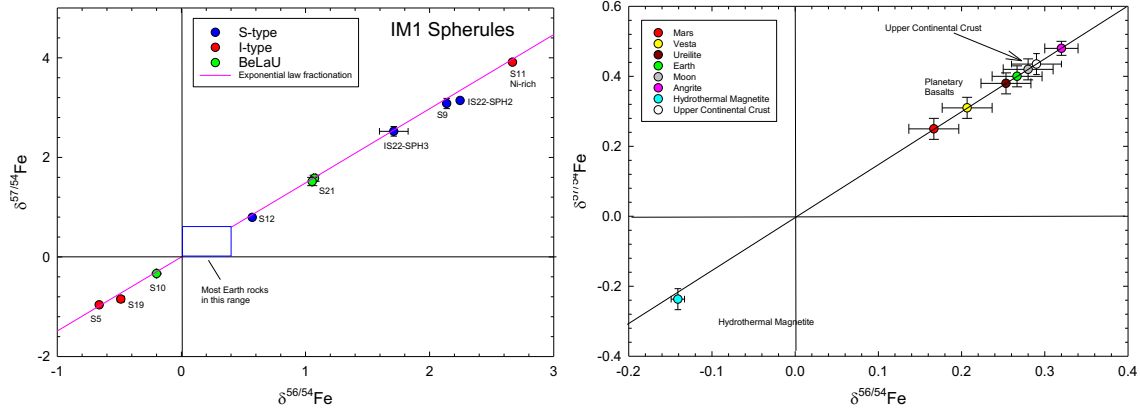


Figure 17. $\delta^{57/54}\text{Fe}$ versus $\delta^{56/54}\text{Fe}$ for spherules in Table 6. All spherules lie outside the box in the diagram of the left panel. This box corresponds to most terrestrial igneous rocks, with detail shown on the right panel, including planetary basalts summarized by Sossi et al. (2016) and Ni et al. (2020). The upper continental crust estimate is from Gong et al. (2017).

Mass spectrometric measurements of spherules along IM1’s path shows high enrichment of Be, La and U, with extremely strong enrichment of refractory lithophile elements, very low refractory siderophile elements such as Re. Volatile elements, such as Mn, Zn and Pb, were most likely lost by evaporation during IM1’s passage through the Earth’s lower atmosphere. In addition, relatively large mass-dependent iron isotope variations ($^{56}\text{Fe}/^{54}\text{Fe}$ correlated with $^{57}\text{Fe}/^{54}\text{Fe}$), supports evaporative losses from IM1’s spherules during atmospheric passage.

Spherules with the “BeLaU” abundance pattern shown in Figs. 12-16 were found only along IM1’s path and not in control regions. The “BeLaU” elemental abundance pattern does not match terrestrial alloys, fallout from nuclear explosions (Wannier et al., 2019), magma ocean abundances of Earth, its Moon or Mars or other natural meteorites in the solar system. This supports the interstellar origin of IM1 independently of the measurement of its high speed, as reported in the CNEOS catalog (Siraj and Loeb, 2022a) and confirmed by the US Space Command⁵.

Since IM1’s spherules melted off the surface of the object, the enhanced Be abundance might represent a flag of cosmic-ray spallation on IM1’s surface along a extended interstellar journey through the Milky-Way galaxy (Johnson, 2019; Yokoyama and Walker, 2016; Gyngard et al., 2009; Hedman, 2019). This constitutes a fourth indicator of an interstellar origin to IM1, in addition to its high speed, its heavy element composition and its iron isotope ratios. The enhanced abundances of heavy elements may explain the high material strength inferred for IM1 based on the high ram-pressure it was able to sustain before disintegrating (Siraj and Loeb, 2022b). The high material strength inferred for IM1 can potentially be tested experimentally by assembling a material mix based on the “BeLaU” composition (Sunder et al., 2001), with proper compensation for lost volatile elements.

The “BeLaU” abundance pattern suggests that IM1 may have originated from a highly differentiated crust of a planet with an iron core outside the solar system. In that case, IM1’s high speed of $\sim 60 \text{ km s}^{-1}$ in the Local Standard of Rest of the Milky-

⁵<https://web.cfa.harvard.edu/loeb/DoD.pdf>

Way galaxy (Siraj and Loeb, 2022a) and the extremely large number of similar objects per star, $\sim 10^{23\pm 1}$, inferred statistically for the population of natural interstellar objects it represents (cf. Fig. 3 in Siraj and Loeb (2022b)), are challenging to explain by common dynamical processes. The “BeLaU” overabundance of heavy elements could perhaps have instead originated from r -process enrichment and fragmentation of ejecta from core-collapse supernovae or neutron star mergers (Radice et al., 2018; Johnson, 2019; Siegel, 2022; Fujibayashi et al., 2023). However, the “BeLaU” pattern also displays s -process enrichment which must have a separate origin, such as Asymptotic Giant Branch (AGB) stars (Busso et al., 1999; Bisterzo et al., 2011; Karakas et al., 2012). Another possibility is that this unfamiliar abundance pattern may reflect an extraterrestrial technological origin. These interpretations will be considered critically along with additional results from spherule analysis in future publications.

Author contributions. A. Loeb served as the chief scientist of the expedition, which was coordinated by R. McCallum and funded by C. Hoskinson. Other co-authors contributed to various aspects of the expedition, the collection of materials with the magnetic sled and the analysis of these materials.

Competing interests. No competing interests.

Acknowledgements. We thank C. Hoskinson for funding the expedition and the Galileo Project at Harvard University for administrative and research support. We are also grateful to Morgan MacLeod, Hamsa Padmanabhan and John Raymond for helpful comments on the manuscript.

References

- Agarwal, D. K. and Palayil, J. K.: Recovery of hydrothermal wustite-magnetite spherules from the Central Indian Ridge, Indian Ocean, *Scientific Reports*, 12, 6811, <https://doi.org/10.1038/s41598-022-10756-1>, 2022.
- Bisterzo, S., Gallino, R., Straniero, O., Cristallo, S., and Käppeler, F.: The s-process in low-metallicity stars–II. Interpretation of high-resolution spectroscopic observations with asymptotic giant branch models, *Monthly Notices of the Royal Astronomical Society*, 418, 284–319, <https://doi.org/10.1111/j.1365-2966.2011.19484.x>, 2011.
- Brownlee, D., Bates, B., and Schramm, L.: The Leonard Award address presented 1996 July 25, Berlin, Germany: The elemental composition of stony cosmic spherules, *Meteoritics & Planetary Science*, 32, 157–175, 1997.
- Brownlee, D. E., Pilachowski, L. B., and Hodge, P. W.: Meteorite Mining on the Ocean Floor, in: *Lunar and Planetary Science Conference*, Lunar and Planetary Science Conference, pp. 157–158, 1979.
- Busso, M., Gallino, R., and Wasserburg, G. J.: Nucleosynthesis in Asymptotic Giant Branch Stars: Relevance for Galactic Enrichment and Solar System Formation, *Annual Review of Astronomy and Astrophysics*, 37, 239–309, <https://doi.org/10.1146/annurev.astro.37.1.239>, 1999.
- Engrand, C., McKeegan, K. D., Leshin, L. A., Herzog, G. F., Schnabel, C., Nyquist, L. E., and Brownlee, D. E.: Isotopic compositions of oxygen, iron, chromium, and nickel in cosmic spherules: Toward a better comprehension of atmospheric entry heating effects, *Geochimica et Cosmochimica Acta*, 69, 5365–5385, 2005.
- Folco, L., Cordier, C., et al.: Micrometeorites, *EMU Notes in Mineralogy*, 15, 253–297, 2015.
- Fujibayashi, S., Kiuchi, K., Wanajo, S., Kyutoku, K., Sekiguchi, Y., and Shibata, M.: Comprehensive Study of Mass Ejection and Nucleosynthesis in Binary Neutron Star Mergers Leaving Short-lived Massive Neutron Stars, *The Astrophysical Journal*, 942, 39, <https://doi.org/10.3847/1538-4357/ac9ce0>, 2023.
- Genge, M. J., Engrand, C., Gounelle, M., and Taylor, S.: The classification of micrometeorites, *Meteoritics & Planetary Science*, 43, 497–515, 2008.
- Genge, M. J., Davies, B., Suttle, M. D., van Ginneken, M., and Tomkins, A. G.: The mineralogy and petrology of I-type cosmic spherules: Implications for their sources, origins and identification in sedimentary rocks, *Geochimica et Cosmochimica Acta*, 218, 167–200, <https://doi.org/10.1016/j.gca.2017.09.004>, 2017.
- Genge, M. J., Davies, B., Suttle, M. D., van Ginneken, M., and Tomkins, A. G.: The mineralogy and petrology of I-type cosmic spherules: Implications for their sources, origins and identification in sedimentary rocks, *Geochimica et Cosmochimica Acta*, 218, 167–200, 2017.
- Giuliani, A., Pearson, D. G., Soltys, A., Dalton, H., Phillips, D., Foley, S. F., Lim, E., Goemann, K., Griffin, W. L., and Mitchell, R. H.: Kimberlite genesis from a common carbonate-rich primary melt modified by lithospheric mantle assimilation, *Science Advances*, 6, eaaz0424, 2020.
- Gong, Y., Xia, Y., Huang, F., and Yu, H.: Average iron isotopic compositions of the upper continental crust: constrained by loess from the Chinese Loess Plateau, *Acta Geochimica*, 36, 125–131, 2017.
- Gyngard, F., Amari, S., Zinner, E., and Ott, U.: Interstellar exposure ages of large presolar SiC grains from the Murchison meteorite, *The Astrophysical Journal*, 694, 359, 2009.
- Hedman, M.: Using cosmogenic Lithium, Beryllium and Boron to determine the surface ages of icy objects in the outer solar system, *Icarus*, 330, 1–4, 2019.

- Herzog, G., Xue, S., Hall, G., Nyquist, L., Shih, C.-Y., Wiesmann, H., and Brownlee, D.: Isotopic and elemental composition of iron, nickel, and chromium in type I deep-sea spherules: Implications for origin and composition of the parent micrometeoroids, *Geochimica et Cosmochimica Acta*, 63, 1443–1457, 1999.
- Herzog, G. F. H., Xue, S., Hall, G. S., Nyquist, L. E., Shih, C. Y., Wiesmann, H., and Brownlee, D. E.: Isotopic and elemental composition of iron, nickel, and chromium in type I deep-sea spherules: Implications for origin and composition of the parent micrometeoroids, *Geochimica et Cosmochimica Acta*, 63, 1443–1457, [https://doi.org/10.1016/S0016-7037\(99\)00011-3](https://doi.org/10.1016/S0016-7037(99)00011-3), 1999.
- Jambon, A., Barrat, J., Sautter, V., Gillet, P., Göpel, C., Javoy, M., Joron, J., and Lesourd, M.: The basaltic shergottite Northwest Africa 856: Petrology and chemistry, *Meteoritics & Planetary Science*, 37, 1147–1164, 2002.
- Johnson, J. A.: Populating the periodic table: Nucleosynthesis of the elements, *Science*, 363, 474–478, <https://doi.org/10.1126/science.aau9540>, 2019.
- Karakas, A. I., García-Hernández, D. A., and Lugaro, M.: Heavy Element Nucleosynthesis in the Brightest Galactic Asymptotic Giant Branch Stars, *The Astrophysical Journal*, 751, 8, <https://doi.org/10.1088/0004-637X/751/1/8>, 2012.
- Kitts, K. and Lodders, K.: Survey and evaluation of eucrite bulk compositions, *Meteoritics and Planetary Science Supplement*, 33, 197–213, 1998.
- Kitts, K. and Lodders, K.: Survey and evaluation of eucrite bulk compositions, *Meteoritics & Planetary Science*, 33, A197–A213, 1998.
- Lodders, K.: A survey of shergottite, nakhlite and chassigny meteorites whole-rock compositions, *Meteoritics & Planetary Science*, 33, A183–A190, 1998.
- Maurette, M., Olinger, C., Michel-Levy, M. C., Kurat, G., Pourchet, M., Brandstätter, F., and Bourot-Denise, M.: A collection of diverse micrometeorites recovered from 100 tonnes of Antarctic blue ice, *Nature*, 351, 44–47, 1991.
- Ni, P., Chabot, N. L., Ryan, C. J., and Shahar, A.: Heavy iron isotope composition of iron meteorites explained by core crystallization, *Nature geoscience*, 13, 611–615, 2020.
- Radice, D., Perego, A., Hotokezaka, K., Fromm, S. A., Bernuzzi, S., and Roberts, L. F.: Binary Neutron Star Mergers: Mass Ejection, Electromagnetic Counterparts, and Nucleosynthesis, *The Astrophysical Journal*, 869, 130, <https://doi.org/10.3847/1538-4357/aaf054>, 2018.
- Rochette, P., Folco, L., Suavet, C., van Ginneken, M., Gattacceca, J., Perchiazzi, N., Braucher, R., and Harvey, R. P.: Micrometeorites from the Transantarctic Mountains, *Proceedings of the National Academy of Science*, 105, 18 206–18 211, <https://doi.org/10.1073/pnas.0806049105>, 2008.
- Rudnick, R. and Gao, S.: The Composition of the Continental Crust, *The Crust, Treatise on Geochemistry*, 3, 2014.
- Rudraswami, N., Prasad, M. S., Dey, S., Plane, J., Feng, W., and Taylor, S.: Evaluating changes in the elemental composition of micrometeorites during entry into the earth’s atmosphere, *The Astrophysical Journal*, 814, 78, 2015.
- Russell, W., Papanastassiou, D., and Tombrello, T.: Ca isotope fractionation on the Earth and other solar system materials, *Geochimica et cosmochimica acta*, 42, 1075–1090, 1978.
- Siegel, D. M.: r-Process nucleosynthesis in gravitational-wave and other explosive astrophysical events, *Nature Reviews Physics*, 4, 306–318, <https://doi.org/10.1038/s42254-022-00439-1>, 2022.
- Siraj, A. and Loeb, A.: A Meteor of Apparent Interstellar Origin in the CNEOS Fireball Catalog, *The Astrophysical Journal*, 939, 53, <https://doi.org/10.3847/1538-4357/ac8eac>, 2022a.
- Siraj, A. and Loeb, A.: Interstellar Meteors Are Outliers in Material Strength, *The Astrophysical Journal Letters*, 941, L28, <https://doi.org/10.3847/2041-8213/aca8a0>, 2022b.

- Siraj, A. and Loeb, A.: Localizing The First Interstellar Meteor With Seismometer Data, arXiv e-prints, arXiv:2303.07357, <https://doi.org/10.48550/arXiv.2303.07357>, 2023.
- Sossi, P. A., Nebel, O., Anand, M., and Poitrasson, F.: On the iron isotope composition of Mars and volatile depletion in the terrestrial planets, *Earth and Planetary Science Letters*, 449, 360–371, 2016.
- Sunder, S., McEachern, R., and LeBlanc, J. C.: High-temperature, Knudsen cell-mass spectroscopic studies on lanthanum oxide/uranium dioxide solid solutions, *Journal of Nuclear Materials*, 294, 59–63, [https://doi.org/10.1016/S0022-3115\(01\)00454-8](https://doi.org/10.1016/S0022-3115(01)00454-8), 2001.
- Taylor, S. and Brownlee, D. E.: Cosmic Spherules in the Geologic Record, *Meteoritics*, 26, 203, <https://doi.org/10.1111/j.1945-5100.1991.tb01040.x>, 1991.
- Taylor, S., Lever, J. H., and Harvey, R. P.: Numbers, types, and compositions of an unbiased collection of cosmic spherules, *Meteoritics & Planetary Science*, 35, 651–666, 2000.
- Tillinghast-Raby, A., Loeb, A., and Siraj, A.: Expected Fragment Distribution from the First Interstellar Meteor C NEOS 2014-01-08, arXiv e-prints, arXiv:2212.00839, 2022.
- Vondrak, T., Plane, J., Broadley, S., and Janches, D.: A chemical model of meteoric ablation, *Atmospheric Chemistry and Physics*, 8, 7015–7031, 2008.
- Wannier, M. M. A., de Urreiztieta, M., Wenk, H.-R., Stan, C. V., Tamura, N., and Yue, B.: Fallout melt debris and aerodynamically-shaped glasses in beach sands of Hiroshima Bay, Japan, *Anthropocene*, 25, 100196, <https://doi.org/10.1016/j.ancene.2019.100196>, 2019.
- Warren, P. H.: KREEP: major-element diversity, trace-element uniformity (almost)., in: *Moon in transition: Apollo 14, KREEP, and evolved lunar rocks*, pp. 149–153, 1989.
- Wittke, J. H., Weaver, J. C., Bunch, T. E., Kennett, J. P., Kennett, D. J., Moore, A. M., Hillman, G. C., Tankersley, K. B., Goodyear, A. C., Moore, C. R., et al.: Evidence for deposition of 10 million tonnes of impact spherules across four continents 12,800 y ago, *Proceedings of the National Academy of Sciences*, 110, E2088–E2097, 2013.
- Xue, S., Herzog, G. F., Hall, G. S., and Brownlee, D. E.: Nickel Isotope Fractionation in Metal Oxide Deep-Sea Spheres With and Without Metal Cores, *Meteoritics*, 29, 553, 1994.
- Yokoyama, T. and Walker, R. J.: Nucleosynthetic Isotope Variations of Siderophile and Chalcophile Elements in the Solar System, *Reviews in Mineralogy and Geochemistry*, 81, 107–160, <https://doi.org/10.2138/rmg.2016.81.03>, 2016.

Appendix A: Elemental data normalized to CI chondrites from the Harvard Laboratory.

Val/top label	Sphere name	Run #	Type	Subclass	Calculated mass (mg)	density	Diameter (mm)	Li	Be	Na	Mg	Al	P	K	Ca	Sc	Ti	V	Cr	Mn	Fe	Co	
S10	IS4 SPH1	4	D-type	Bel-Au	0.327	5	0.500	56.474	587.997	2.773	0.029	10.209	0.368	8.528	3.317	6.243	11.480	3.035	0.053	0.134	2.856	0.076	
no label	IS4 SPH1	14	D-type	Bel-Au	1.727	5	0.871	41.479	398.073	0.524	0.023	6.207	0.805	2.420	1.334	3.590	6.259	1.783	0.491	0.029	3.002	0.083	
no label	(6) IS13 SPH4	4	D-type	Bel-Au	9.218	5	1.572	58.029	398.501	1.580	0.030	10.571	0.132	4.079	1.720	7.424	11.582	3.897	0.288	0.101	2.912	0.062	
no label	(9) IS4 SPH4	4	D-type	Bel-Au	0.847	5	0.687	19.902	1296.240	0.795	0.020	10.242	0.488	4.969	0.313	2.466	5.750	1.012	0.031	0.042	2.871	0.038	
no label	(25) IS13 SPH3	13	D-type	Bel-Au	2.087	3.5	1.045	80.262	4587.457	2.634	0.090	27.291	0.404	21.584	10.950	13.618	16.159	5.710	0.004	0.277	1.314	0.062	
no label	IS4 SPH2	14	D-type	Low-La	2.681	5	1.008	66.099	125.328	1.583	0.108	5.313	0.406	5.596	2.598	8.824	10.249	3.644	0.177	0.146	3.116	0.046	
no label	IS4 SPH3	14	D-type	Low-La	0.209	5	0.431	78.784	94.904	0.182	0.065	6.201	0.241	4.077	2.226	1.748	7.575	2.004	0.024	0.102	3.179	0.029	
no label	IS17 SPH1	17	D-type	Low-La	0.096	5	0.332	16.411	58.524	12.394	0.333	24.231	3.195	49.140	15.122	7.547	12.662	5.952	0.033	1.252	0.664	0.069	
no label	(1) IS17 SPH1	22	D-type	Low-La	9.979	3.5	1.760	4.134	17.053	1.634	0.012	0.996	0.097	5.428	0.435	5.747	390.979	5.533	0.300	24.913	2.855	0.067	
no label	(3) IS13 SPH1	13	D-type	Low-La	1.579	5	0.845	25.068	19.883	0.410	0.109	5.038	0.824	17.871	2.826	10.954	1.902	2.191	0.015	8.245	3.059	0.027	
no label	(11) IS14 SPH11	14	D-type	Low-La	0.250	5	0.457	12.697	252.588	1.331	0.109	0.996	0.824	17.871	2.826	10.954	1.902	2.191	0.015	8.245	3.059	0.027	
no label	(13) IS17 SPH3	17	D-type	Low-La	0.270	3.5	0.528	13.325	61.174	9.886	0.275	14.091	1.670	40.441	32.839	5.778	13.047	6.397	0.007	1.297	0.583	0.078	
no label	(14) IS17 SPH4	17	D-type	Low-La	0.583	3.5	0.683	16.260	56.898	12.383	0.287	24.193	3.190	47.640	13.039	6.355	16.988	10.448	0.024	1.194	0.346	0.066	
no label	(15) IS17 SPH5	17	D-type	Low-La	0.383	3.5	0.593	11.676	48.603	8.397	0.252	14.338	1.539	40.612	34.100	5.060	13.223	6.066	0.011	1.197	0.566	0.073	
no label	(17) IS4 SPH7	4	D-type	Low-La	0.575	5	0.761	3.656	104.969	0.196	0.096	1.249	0.288	2.961	0.757	5.358	87.128	33.535	0.014	2.712	3.331	0.235	
no label	(18) IS4 SPH8	4	D-type	Low-La	1.151	5	0.604	1.314	80.508	0.308	0.205	4.067	1.556	1.635	0.710	2.068	4.732	1.622	0.015	6.515	0.544	0.029	
no label	(21) IS8 SPH8	8	D-type	Low-La	0.822	5	0.680	25.840	80.508	0.308	0.205	4.067	1.556	1.635	0.710	2.068	4.732	1.622	0.015	6.515	0.544	0.029	
no label	(28) IS13 SPH8b	13	D-type	Low-La	4.058	3.5	1.304	15.373	81.292	9.877	0.336	22.527	2.882	46.208	14.354	8.349	16.787	8.874	0.011	1.658	0.854	0.099	
no label	(30) IS13 SPH12	13	D-type	Low-La	1.982	5	0.912	0.809	1.202	0.414	0.115	1.668	2.690	1.098	0.787	6.333	108.857	41.976	0.037	2.638	3.259	0.225	
no label	(31) IS14 SPH5	14	D-type	Low-La	1.688	5	0.864	1.371	0.244	0.420	0.084	1.601	1.019	1.303	0.126	6.681	90.957	17.202	0.002	3.740	3.372	0.166	
no label	(32) IS14 SPH6	14	D-type	Low-La	0.425	5	0.546	191.968	60.518	2.787	0.072	6.590	0.028	3.076	1.068	0.174	3.837	2.215	0.021	0.312	3.158	0.050	
no label	IS13 SPH3	13	E-type	Ni-rich	0.146	5	0.383	0.000	0.000	0.150	0.002	0.201	0.072	1.133	0.905	0.000	0.929	1.400	1.945	0.002	3.660	4.952	
S11	IS13 SPH2	4	E-type	Ni-rich	0.097	5	0.333	0.000	0.000	0.095	0.195	0.288	0.103	1.016	0.325	0.210	0.212	0.188	0.107	3.251	8.257		
no label	(12) IS14 SPH14	14	E-type	Ni-rich	0.496	5	0.575	0.000	0.000	0.133	0.006	0.236	0.326	1.758	0.000	0.433	1.593	2.427	0.005	3.551	6.203		
no label	(24) IS8 SPH6	8	E-type	Ni-rich	0.832	5	0.682	0.000	0.000	0.037	0.001	0.107	0.055	0.077	0.000	0.000	0.000	0.168	0.089	0.007	3.739	5.533	
S16	IS12 SPH1	12	E-type	Ni, Mn-poor	0.902	5	0.701	25.156	0.125	0.003	0.989	0.034	0.663	0.270	0.082	0.306	0.072	0.002	0.006	3.723	0.015		
no label	IS8 SPH1	8	E-type	Ni-poor	0.497	5	0.575	0.000	0.101	0.306	0.569	0.735	1.126	1.399	1.567	0.009	1.426	3.122	0.013				
no label	IS8 SPH2	8	E-type	Ni-poor	0.117	5	0.355	0.000	0.000	0.066	0.008	0.146	0.384	1.103	1.568	0.000	0.618	0.140	0.076	2.210	3.676	0.065	
S7	IS16 SPH2	16	E-type	Ni-poor	0.836	5	0.684	0.000	0.000	0.110	0.002	0.040	0.096	0.277	0.124	0.064	0.340	0.029	0.320	3.762	0.016		
S23	IS19 SPH1	19	E-type	Ni-poor	0.116	5	0.354	0.000	0.000	0.107	0.006	0.047	0.266	1.088	1.726	0.000	0.018	0.075	0.085	2.348	3.681	0.034	
S29	IS19 SPH7	19	E-type	Ni-poor	0.157	5	0.392	0.000	0.000	0.164	0.040	0.183	0.205	0.732	1.673	0.000	0.183	0.370	0.144	2.173	3.662	0.022	
S31	IS19 SPH8	19	E-type	Ni-poor	0.119	5	0.357	0.000	0.000	0.042	0.040	9.711	0.190	0.963	0.908	0.000	1.697	0.669	0.084	0.433	3.084	0.037	
S5	IS8 SPH8	8	E-type	Ni-poor	0.246	5	0.455	0.825	7.976	0.077	0.004	0.099	0.173	0.467	0.194	0.066	1.513	0.572	0.096	1.328	3.759	0.122	
S19	IS13 SPH2	13	E-type	Ni-poor	0.495	5	0.574	0.213	0.000	0.041	0.003	0.022	0.057	0.321	0.064	0.030	0.734	0.126	0.095	2.194	3.752	0.016	
no label	(2) IS22 SPH4	22	E-type	Ni-poor	4.643	5	1.211	0.134	0.487	0.077	0.001	0.013	0.147	0.055	0.278	1.131	0.904	0.167	2.092	3.763	0.054		
no label	(9) IS13 SPH9	13	E-type	Ni-poor	2.840	5	1.028	0.113	0.335	0.031	0.003	0.017	0.035	0.069	0.000	0.000	0.000	0.014	0.029	1.827	3.742	0.024	
no label	(10) IS14 SPH10	14	E-type	Ni-poor	0.777	5	0.667	6.184	0.000	0.103	0.003	0.066	0.195	0.707	0.655	0.000	0.000	0.014	0.029	1.827	3.742	0.024	
no label	(22) IS8 SPH4	8	E-type	Ni-poor	0.615	5	0.617	0.490	0.000	0.353	0.106	2.049	0.380	0.410	0.000	4.999	69.961	47.738	0.011	1.606	3.388	0.290	
no label	(26) IS13 SPH6	13	E-type	Ni-poor	2.068	5	0.925	0.000	0.000	0.064	0.001	0.042	0.043	0.000	0.000	0.000	0.000	0.000	0.035	0.026	1.574	3.790	0.031
no label	IS4 SPH4	4	E-type	Chondritic	0.149	3.5	0.434	1.09	0.00	1.91	1.79	0.48	0.45	1.26	1.56	1.11	1.11	0.76	1.04	0.83	1.06	0.65	
no label	IS4 SPH5	4	E-type	Chondritic	0.071	3.5	0.338	0.000	0.000	0.966	1.745	1.869	0.473	2.988	4.536	1.182	1.580	1.079	0.287	0.924	0.917	0.247	
no label	IS13 SPH4	13	E-type	Chondritic	0.122	3.5	0.405	6.897	6.233	1.284	1.679	1.128	0.466	2.347	1.089	2.556	0.737	2.292	3.327	1.668	1.168	0.317	
no label	IS17 SPH2	17	E-type	Chondritic	0.075	3.5	0.345	0.152	0.000	0.036	1.429	1.142	1.042	6.731	2.350	2.619	2.612	2.029	2.991	0.683	1.334	1.341	
S25	IS19 SPH2	19	E-type	Chondritic	0.078	3.5	0.351	0.503	0.000	0.384	1.481	0.931	1.831	6.784	3.526	0.831	1.168	1.157	1.421	0.960	1.425	1.151	
no label	IS19 SPH3	19	E-type	Chondritic	0.156	3.5	0.440	1.719	0.000	0.037	1.481	1.771	0.388	2.053	1.580	1.531	1.612	1.496	1.666	1.054	1.414	1.393	
S9	IS4 SPH5	4	E-type	Chondritic	0.156	3.5	0.440	1.290	0.000	0.031	1.630	1.779	0.180	1.448	1.722	1.555	1.228	0.953	0.924	1.124	1.144	1.333	
no label	IS27 SPH2	22	E-type	Chondritic	0.027	3.5	0.244	5.627	0.000	0.128	1.571	1.295	0.363	7.035	2.307	2.626	2.142	1.112	1.031	0.981	1.291	1.295	
no label	IS27 SPH3	22	E-type	Chondritic	0.029	3.5	0.251	2.122	132.729	0.153	1.663	1.198	0.625	6.143	2.007	1.687	0.491	1.145	1.435	0.996	1.164	1.144	
no label	(4) IS13 SPH11	13	E-type	Chondritic	0.639	3.5	0.704	3.190	0.326	0.152	1.798	0.651	0.521	0.739	0.417	0.935	1.098	1.162	1.640	1.089	0.927		
no label	(7) IS14 SPH7	14	E-type	Chondritic																			

	11000	126	312	10	32.7	1.86	18.6	2.3	7.8	1.56	3.94	0.246	0.928	0.199	0.686	0.142	0.187	2.34	0.235	0.603	0.089	0.452	0.147	0.056
NI	Cu	Zn	Ga	Ge	As	Se	Rb	Sr	Y	Zr	Nb	Mo	Ag	Cd	Sb	Cs	Ba	La	Ce	Pr	Nd	Sm	Eu	
0.011	0.9271	0.40	4.228	0.258	1.108	0.013	7.666	57.323	86.311	118.105	155.413	5.267	1.220	0.130	8.996	5.845	390.556	282.298	212.856	162.858	128.678	84.407	47.932	
0.007	0.428	0.029	2.723	0.290	0.558	0.014	1.977	287.536	77.024	62.672	61.478	83.479	0.373	0.075	0.333	0.987	324.316	678.173	443.582	288.190	197.700	108.798	58.215	
0.003	0.723	0.000	2.023	0.282	0.757	0.013	2.945	355.175	85.221	158.857	140.412	21.347	1.044	0.091	3.874	1.954	620.711	345.466	251.486	187.158	150.509	106.233	59.807	
0.005	0.000	0.000	6.118	0.129	7.019	0.013	6.063	16.484	120.624	50.456	24.460	0.544	0.020	4.773	10.287	97.450	375.241	299.634	228.001	189.090	126.621	57.059		
0.018	0.956	0.000	6.875	0.150	2.279	0.038	20.295	82.837	312.070	64.529	34.471	193.072	1.451	0.330	16.571	30.347	1217.031	1108.018	747.397	559.576	452.667	309.323	158.385	
0.003	0.302	0.103	1.848	0.302	0.478	0.004	5.154	83.489	24.520	64.825	123.329	37.200	0.448	0.000	6.098	269.272	82.103	68.753	54.888	43.703	29.836	18.298		
0.003	1.127	0.477	0.557	0.291	0.332	0.004	2.168	65.168	14.771	25.362	50.718	7.305	0.459	0.161	4.804	1.680	277.740	148.834	105.183	78.669	55.540	29.628	14.917	
0.012	1.658	0.978	3.372	0.066	6.531	0.002	26.256	172.991	27.329	28.700	23.554	6.626	0.098	0.167	7.384	9.077	303.748	85.346	73.563	68.653	56.121	36.479	43.304	
0.001	0.550	0.773	1.813	0.100	0.771	0.016	2.628	14.115	76.928	13.863	3.439	0.583	0.113	0.035	0.617	0.837	33.963	70.296	81.813	99.034	117.467	118.712	68.519	
0.008	1.456	8.018	0.767	0.268	0.848	0.001	7.728	2.915	21.340	264.000	1179.701	70.357	1.546	0.159	10.267	0.000	24.804	40.215	32.282	28.111	22.593	15.655	10.028	
0.003	1.289	0.000	1.611	0.295	0.855	-0.003	7.039	15.266	54.214	26.558	12.864	19.156	0.026	0.000	13.122	0.537	148.589	25.063	41.719	49.908	66.291	74.962	51.037	
0.002	2.331	0.000	2.367	0.068	2.370	0.006	20.695	272.899	25.579	21.713	0.000	2.818	0.000	0.072	0.000	12.626	211.751	83.825	64.049	68.353	66.093	47.095	34.107	
0.016	1.663	0.000	3.458	0.085	6.576	0.005	24.507	176.651	24.951	28.950	14.526	7.615	0.332	2.503	10.718	11.027	381.925	85.079	65.236	63.117	61.529	38.332	40.595	
0.002	2.468	0.000	2.375	0.054	1.812	0.002	21.716	385.939	25.201	24.674	3.555	3.302	0.301	0.306	2.379	13.245	206.262	83.930	64.168	61.571	60.332	44.008	36.605	
0.001	2.443	0.000	2.922	0.279	0.866	0.001	0.747	15.050	12.544	9.368	22.560	18.403	0.000	0.000	8.483	0.180	28.903	24.406	28.447	23.257	21.115	19.161	14.708	
0.003	0.097	1.597	4.430	0.327	0.666	0.003	1.330	3.843	31.922	7.449	2.990	3.473	0.076	0.000	2.942	2.241	54.976	68.077	60.806	45.484	39.487	18.850	12.010	
0.006	0.499	0.000	2.387	0.290	0.634	0.004	1.627	17.028	11.887	26.039	27.645	15.907	0.010	0.000	1.292	2.241	54.976	68.077	60.806	45.484	39.487	18.850	12.010	
0.009	2.274	0.648	3.656	0.086	6.567	0.007	24.627	184.005	31.529	32.099	12.947	2.646	0.160	1.987	3.123	14.968	251.610	101.570	88.221	84.838	77.692	58.879	46.736	
0.001	0.115	2.334	3.916	0.315	0.231	0.002	0.487	3.507	10.795	5.370	5.410	0.940	0.000	0.012	0.000	0.108	8.291	16.369	17.588	19.677	22.478	20.459	9.320	
0.004	0.320	3.444	4.168	0.322	0.409	0.000	0.742	3.303	4.427	3.641	2.688	1.735	0.052	0.078	0.000	0.538	23.346	11.633	15.589	11.224	12.146	9.932	4.275	
0.008	0.500	0.000	1.804	0.300	0.340	-0.005	2.447	110.241	5.804	7.230	5.956	2.534	0.202	0.000	0.072	1.610	596.484	47.489	30.450	22.079	18.429	12.895	11.249	
1.093	0.095	0.363	0.012	0.341	0.984	0.002	0.110	0.294	0.425	0.660	2.006	2.815	0.242	0.000	26.772	0.147	0.870	0.775	0.483	0.420	0.613	0.314	0.000	
5.181	0.006	0.025	0.030	0.296	2.640	0.014	0.074	0.399	0.045	1.229	0.520	3.992	18.718	0.014	0.551	0.000	0.601	0.035	0.248	0.749	0.300	0.180	0.139	
2.221	0.070	0.000	0.009	0.345	1.085	0.010	0.172	-0.057	0.031	0.184	0.000	2.992	0.392	0.048	2.648	0.000	0.486	0.000	0.000	0.000	0.000	0.000	0.000	
1.498	0.015	0.000	0.011	0.341	0.997	0.017	0.032	0.048	0.048	0.000	1.356	0.000	0.023	0.000	0.000	0.000	0.002	0.000	0.109	0.000	0.000	0.000	0.000	
0.003	0.150	0.042	0.104	0.347	0.190	0.002	0.455	5.981	1.713	0.956	25.045	0.040	0.000	1.471	0.682	56.111	8.517	9.352	8.606	8.016	5.824	2.888		
0.003	1.005	0.020	0.611	0.358	1.754	0.000	0.136	4.202	0.455	0.508	2.954	0.031	0.500	0.125	0.800	0.084	15.334	1.444	6.995	1.431	1.475	0.535	0.457	
0.005	0.729	1.991	0.937	0.349	0.402	0.000	0.102	0.868	0.193	1.692	10.804	15.488	0.389	0.280	15.162	0.184	10.008	1.389	0.726	0.959	5.235	0.817	0.262	
0.001	0.240	0.002	0.830	0.357	0.132	0.000	0.049	0.130	0.034	0.111	74.493	4.919	0.001	0.019	2.550	0.050	0.972	1.110	0.180	0.142	0.641	0.000	0.102	
0.008	0.449	0.004	0.336	0.348	0.839	0.000	0.126	0.522	0.166	0.613	1.810	17.177	0.158	0.140	10.528	0.188	1.312	0.518	0.264	0.210	5.295	0.000	0.000	
0.008	2.166	0.595	0.913	0.334	0.152	0.003	0.021	1.726	0.180	2.481	56.554	17.647	0.055	0.099	9.447	0.266	21.081	0.798	1.022	0.675	0.747	0.000	0.000	
0.004	0.467	0.258	0.276	0.302	0.601	0.000	0.140	0.103	0.879	0.130	16.312	10.418	0.213	0.000	3.088	0.000	1.638	0.909	0.597	0.886	0.746	0.000	0.000	
0.026	4.438	1.119	0.753	0.323	4.566	0.001	0.098	1.059	4.06	1.482	32.474	41.540	7.162	0.121	72.315	0.022	13.400	2.501	1.665	1.387	1.026	0.593	0.268	
0.002	1.542	1.318	0.466	0.323	0.384	0.000	0.049	0.130	0.024	0.215	15.510	12.408	3.282	0.160	9.318	0.000	4.567	0.109	0.128	0.135	0.074	0.000	0.040	
0.013	0.904	0.442	0.898	0.339	0.390	0.000	0.018	0.680	0.079	0.481	7.077	39.800	0.074	0.098	8.821	0.000	6.729	0.384	0.213	0.573	0.610	0.212	0.098	
0.022	5.251	5.905	1.198	0.351	0.859	0.001	0.038	0.138	0.055	2.106	55.098	15.919	0.012	1.044	43.433	0.023	10.836	0.000	0.000	0.000	0.000	0.000	0.000	
0.005	0.533	0.991	0.394	0.362	0.677	0.001	0.084	0.306	-0.006	2.288	0.000	11.232	0.301	0.000	10.386	0.000	10.836	0.000	0.000	0.000	0.000	0.000	0.000	
0.001	0.318	0.551	3.776	0.322	0.213	0.002	0.368	2.689	1.110	2.590	0.000	2.204	0.000	0.000	0.000	0.000	2.780	1.779	1.659	1.640	2.194	1.679	0.789	
0.003	3.150	0.000	0.356	0.349	0.431	0.000	0.034	0.245	0.023	0.102	0.000	9.586	0.000	0.000	69.589	0.039	0.732	0.102	0.447	1.825	1.309	0.005	0.000	
0.13	0.07	0.35	0.26	0.11	0.18	0.01	0.124	0.649	0.898	1.897	5.171	2.003	0.469	0.000	9.548	0.000	3.335	1.407	1.029	0.988	1.831	2.031	0.919	
0.038	0.181	0.521	0.047	0.084	0.137	0.006	0.474	1.500	1.542	1.811	5.875	6.256	0.949	1.113	6.590	0.000	5.453	1.964	1.828	2.706	8.332	0.639	0.814	
0.059	0.697	0.579	0.484	0.120	0.999	0.007	0.522	2.317	0.659	3.301	3.973	0.000	0.390	4.116	0.349	26.495	2.081	3.798	2.642	3.698	0.744	0.951		
1.111	0.080	0.187	0.648	0.121	0.399	0.006	0.092	1.791	2.211	3.379	4.763	6.074	0.018	0.249	2.715	0.292	2.376	2.537	2.354					

Gd	Tb	Dy	Ho	Er	Tm	Yb	Lu	Hf	Ta	W	Re	Tl	Pb	Bi	Th	U
0.197	0.0363	0.243	0.0556	0.159	0.0242	0.163	0.0243	0.104	0.014	0.093	0.0365	0.142	2.47	0.114	0.0294	0.0081
77.670	73.935	71.432	68.128	70.799	74.189	64.831	65.005	104.956	103.715	193.082	0.032	2.268	1.522	0.276	499.973	631.415
90.727	74.906	71.032	66.497	72.919	79.053	73.114	73.803	137.281	144.831	81.001	0.058	0.000	0.137	0.019	286.031	759.004
87.465	80.688	80.503	74.051	86.829	86.063	89.369	85.426	177.187	96.031	47.155	0.051	0.005	0.408	0.000	521.150	948.353
101.331	92.970	96.756	91.442	106.910	111.463	98.133	92.126	59.812	42.558	92.727	0.060	0.000	0.000	0.000	280.983	370.383
262.556	255.703	266.343	274.771	349.919	382.504	402.838	425.615	231.810	188.348	681.122	0.223	0.310	4.247	0.188	388.128	1199.392
25.181	24.004	22.715	21.904	22.903	22.716	22.588	22.711	61.938	54.952	32.682	0.003	0.043	0.339	0.006	257.420	348.150
21.543	16.323	15.303	14.151	13.043	15.013	12.924	18.570	28.924	59.978	16.700	0.212	0.000	0.076	1.230	447.484	531.419
39.252	24.171	33.302	27.531	25.198	31.173	24.966	24.268	33.253	27.935	38.879	0.000	1.364	12.562	0.000	103.608	192.290
111.019	95.988	91.236	78.468	79.618	75.763	67.927	62.768	21.508	3.854	1.325	0.053	0.272	0.745	7.754	591.603	1892.266
15.955	18.262	20.521	21.114	23.893	28.400	26.921	32.383	320.257	2652.825	704.696	0.041	0.096	2.560	0.000	207.868	123.228
62.117	65.439	64.807	55.957	63.625	74.433	66.336	69.408	26.750	0.000	174.713	0.663	0.000	3.084	0.000	150.951	265.037
31.706	29.435	27.242	26.296	25.274	26.487	27.254	30.057	24.704	0.000	2.203	0.000	2.890	13.332	0.000	85.305	171.450
31.211	26.233	24.924	26.783	23.077	26.961	27.058	23.759	36.566	10.700	23.809	0.060	1.868	20.627	0.000	102.322	169.442
35.380	26.026	24.799	22.390	25.496	25.542	25.161	26.945	27.407	0.000	0.709	0.351	1.242	11.877	0.000	86.246	195.554
18.152	17.276	17.802	14.020	14.457	17.392	16.525	13.285	8.888	0.000	36.987	0.088	0.000	0.545	0.000	39.516	85.953
63.807	46.409	39.360	35.451	31.374	29.762	21.441	21.753	6.335	0.000	0.000	0.090	0.000	0.958	0.000	10.196	16.631
14.847	13.956	12.293	12.226	13.666	12.273	10.957	13.022	24.515	13.402	34.931	2.057	0.000	0.726	0.000	150.951	265.037
44.358	37.778	35.553	31.698	34.100	34.703	33.723	33.500	38.215	13.068	67.905	0.041	1.999	9.202	1.109	123.687	228.292
19.481	14.523	12.924	11.569	10.559	9.473	7.507	7.385	6.838	1.654	-0.136	0.053	0.025	0.327	0.000	4.563	11.255
7.953	5.487	5.089	4.429	4.179	3.963	4.250	3.173	5.247	0.000	5.247	0.042	2.099	3.798	0.110	5.442	14.689
9.291	5.773	5.751	5.850	6.140	6.599	5.978	6.622	6.622	0.000	58.782	0.003	0.000	2.411	0.000	96.075	145.672
0.000	0.689	0.083	0.363	0.348	0.403	0.124	2.757	0.506	0.000	30.409	0.927	0.015	1.130	0.000	2.128	2.771
0.021	0.048	0.034	0.027	0.061	0.038	0.081	0.151	0.832	1.323	13.099	0.869	0.000	0.257	0.000	0.576	0.000
0.128	0.000	0.154	0.010	0.081	0.000	0.220	3.928	0.000	0.000	58.980	0.349	0.000	2.726	0.000	1.983	0.000
0.150	0.229	0.092	0.099	0.245	0.214	0.065	0.322	0.000	0.000	29.528	0.001	0.000	0.279	0.000	0.040	0.000
5.241	4.450	4.386	4.236	3.798	4.195	3.393	3.443	2.001	1.448	1160.402	0.025	1.756	0.244	0.092	9.399	14.247
0.455	0.351	0.268	0.200	0.167	0.614	0.298	0.467	1.595	21.435	0.001	0.093	18.683	0.004	0.927	36.213	0.000
0.168	0.171	0.217	0.006	0.113	0.000	0.000	1.364	0.867	5.519	21.946	28.296	0.101	0.896	2.869	4.925	7.710
0.023	0.000	0.014	0.045	0.015	0.033	0.000	0.000	0.059	1.974	20.429	0.009	0.000	9.263	0.000	0.388	0.910
0.000	0.000	0.106	0.007	0.110	0.000	0.159	1.331	1.285	0.000	94.777	0.192	0.016	0.000	0.407	1.471	0.171
0.366	0.291	0.226	0.242	0.237	0.535	0.000	0.308	2.444	23.640	41.074	0.003	0.052	0.000	0.000	6.657	5.961
0.166	0.336	0.000	0.330	0.107	0.229	0.000	0.000	1.002	10.994	22.272	0.180	0.000	0.000	1.038	0.476	13.476
0.481	0.435	0.399	0.381	0.310	0.344	0.428	1.923	1.813	18.033	90.053	0.014	0.000	5.793	0.848	9.900	12.804
0.014	0.022	0.040	0.107	0.026	0.050	0.023	0.000	0.154	8.355	43.177	0.002	0.000	83.099	0.472	0.154	0.802
0.142	0.119	0.087	0.116	0.093	0.073	0.034	0.600	0.346	1.130	42.197	0.028	0.000	1.844	0.898	0.608	1.809
0.146	0.021	0.026	0.065	0.027	0.000	0.036	0.359	2.232	25.309	33.262	0.017	0.000	897.120	16.361	0.540	7.684
0.080	0.000	0.049	0.665	0.000	0.000	0.000	3.450	0.258	0.000	6.908	0.266	0.000	1.988	0.000	0.598	0.000
2.439	1.033	1.679	0.454	1.463	1.018	0.801	1.174	1.914	0.000	2.202	0.113	0.000	0.565	0.000	0.751	12.432
0.091	0.000	0.018	0.116	0.119	0.000	0.000	0.272	0.000	0.000	11.814	0.017	0.000	0.268	0.000	0.437	0.300
0.879	0.786	0.461	0.567	0.787	0.758	0.436	2.171	2.506	3.632	5.677	5.531	0.000	0.072	0.000	0.882	0.000
2.472	1.117	2.190	1.092	1.591	0.809	103.946	7.529	2.936	0.000	36.473	7.836	0.000	1.620	0.000	2.354	6.817
0.159	0.488	0.788	0.526	0.821	0.934	1.387	1.966	1.196	0.000	7.737	0.176	1.177	2.040	1.763	0.912	9.368
3.453	2.714	3.129	2.445	2.391	0.392	0.924	1.410	4.654	4.152	7.037	1.054	0.028	0.000	0.000	1.901	0.299
1.006	1.578	1.103	0.180	0.331	0.748	1.131	2.625	4.467	0.000	30.437	0.000	0.029	0.525	0.000	3.640	2.755
1.598	1.217	1.390	1.281	1.351	1.439	1.405	1.434	1.683	3.070	5.542	0.000	0.000	0.326	0.000	0.914	0.000
1.620	1.551	1.539	1.562	1.545	1.936	1.677	2.472	1.762	3.848	3.367	0.000	0.000	0.021	0.000	1.302	0.000
1.131	0.856	1.164	0.964	1.212	1.199	2.043	0.692	1.019	12.220	8.561	0.000	0.000	0.884	0.000	0.000	0.000
0.381	0.554	0.443	0.463	0.892	1.465	0.725	0.970	2.141	0.000	3.422	0.022	0.273	2.730	0.000	1.548	1.921
0.043	0.068	0.027	0.015	0.044	0.000	0.116	-0.017	0.745	0.000	3.473	0.036	0.000	0.479	0.000	0.129	0.000
1.602	0.942	1.188	1.493	1.495	0.733	1.040	2.507	0.745	0.000	144.422	0.046	0.000	1.399	0.000	1.751	0.000
0.960	0.568	1.071	1.156	1.987	1.027	1.470	2.155	0.849	0.000	26.925	0.066	0.000	1.548	0.000	1.333	0.000
2.421	2.670	2.089	1.998	2.443	3.441	2.926	2.945	1.947	0.000	2.894	0.057	0.000	0.394	0.000	2.514	4.033
1.374	1.565	1.480	1.355	1.806	1.521	2.558	37.908	0.644	0.000	0.000	0.376	0.000	0.970	0.000	1.749	0.414
1.579	2.342	1.427	2.043	1.170	1.943	1.647	0.207	1.366	0.000	0.780	0.002	0.000	0.665	0.000	2.347	0.000
1.708	2.853	2.706	1.959	1.630	2.097	2.043	5.003	0.901	0.000	1.722	0.044	0.000	0.419	0.000	2.188	3.290
0.284	0.290	0.644	0.669	0.873	0.678	0.752	1.573	0.000	0.000	19.482	0.080	0.000	1.922	0.000	0.704	6.710

Figure A3. Elemental data normalized to CI. The CI normalizing values are given on top of the table. (Part 3 / 3)

Appendix B: Interstellar process notes: spherule recovery on board M/V Silver Star

B1 ON DECK

B1.1 Collection of components

- 1x Shop vacuum
- 1x Magnetic sled
- 1x 2 L fragment collection containers
- 1x Hose with adjustable spray nozzle and water source
- 1x Logbook and pencil
- 5x Tweezers and fragment recovery implements
- 30 L Collection container, labeled

B1.2 Process notes

- Remove all large fragments by hand using tweezers and recovery implements into 2 L fragment collection container.
- Shop vacuum all remaining sediment from sled into shop vacuum container, adding 10-50 mL of water per magnetic collection disk to collection to provide additional conveyance medium for sediment and fragments. Take care to not directly spray the magnetic sled, or spray only at a highly oblique angle, to ensure sled sediment and fragments are not lost.
- Empty all captured sediment and fragments from shop vacuum container into 30 L collection container.
- Rinse shop vacuum container into 30 L collection container.
- Rinse shop vacuum hose into 30 L collection container.
- Collection container sent to Lab setup Station 1.
- Note time of recovery and sled run number in logbook.

B2 BRIDGE LAB: Wet magnetic separation, Station 1

B2.1 Components

- 1x roll of tape

- 4x quartered pieces of paper
- 1x 30 L Collection container filled with sediment and fragments
- 1x Magnetic plunger for wet use
- 1x 250 mL measuring cup
- 1x "Magnetic particle sieve" sieve (149 micron screen), labeled GP-1100
- 1x 30 L "Magnetic tailings" container, labeled
- 1x Paintbrush
- 50 mL fresh water in measuring cup

B2.2 Process notes

- Collection container placed at Station 1.
- Tape a piece of paper in front of the Collection bucket and name the Collection bucket with the following convention: "[Run Number] - Collection".
- Add 50 mL of fresh water to 250 mL measuring cup.
- Agitate sediment resting at the bottom of the collection container using the paintbrush, making a homogenous aqueous slurry.
- Hold magnetic plunger for wet use into 30L collection container, attracting magnetic sediment.
- Remove magnetic plunger and place in 250 mL measuring cup.
- Release magnetic plunger when submerged in 50 mL of fresh water, releasing magnetic particles into measuring cup.
- Agitate the 50 mL of water and magnetic particles with brush, creating homogenous aqueous slurry.
- Water from 250 mL measuring cup strained through magnetic particle sieve into 30 L magnetic tailings container.
- Tape a piece of paper in front of the magnetic particle sieve with the following convention: "[Run Number] - MAG";
- Keep all water in magnetic tailings container (contains sub-150 micron magnetic tailings).

B3 BRIDGE LAB: Wet non-magnetic particle separation, Station 2

B3.1 Components

- 1x 30 L Collection container with sediment and fragments, less magnetic particles.
- 250 mL measuring cup
- 1x Paintbrush
- 1x "Non-magnetic particle sieve" sieve (300 micron screen)
- 1x 30 L "Non-magnetic tailings" container
- 1x Non-magnetic tailings log and pencil

B3.2 Process Notes

- Collection container placed at Station 2.
- Agitate sediment resting at the bottom of the Collection container using the paintbrush, making a homogenous aqueous slurry.
- Submerge 250 mL measuring cup into Collection container, filling the measuring cup with the aqueous slurry.
- Pour the slurry through the Non-magnetic particle sieve into the Non-magnetic tailings container.
- Tape a piece of paper in front of the Non-magnetic particle sieve and name it with the following convention: "[Run Number] - NMAG".
- Keep all water in Non-magnetic tailings container (contains sub-150-micron magnetic tailings).
- Every 3 hours, remove 750 mL of fresh water off of the top of the Non-magnetic tailings container. (The sediment will settle to the bottom, and you will need room for additional slurry to be added to the Non-magnetic tailings container.)
- Indicate the time in the Non-magnetic tailings when the removal process takes place.

B4 BRIDGE LAB: Sieve drying, Station 3

B4.1 Components

- 1x Non-magnetic particle sieve; sieve (300 micron screen) with sediment
- 1x Magnetic particle sieve; sieve (150 micron screen) with sediment
- 2x small trays that allow for airflow under the sieve
- 10x paper delicate task wipers on underside to assist drying.

B4.2 Process notes

- Place the "Non-magnetic particle sieve" and the "Magnetic particle sieve" on the small trays that allow for airflow both above and over the sieves.
- Let rest for 5-8 hours, periodically blotting the underside of the sieves with delicate task wipers, removing excess moisture.

B5 BRIDGE LAB: Oven firing, Station 4 (Optional, when pressed for time by incoming sled)

B5.1 Components

- 1x oven
- 1x metal cupcake tray
- 1x hot pad
- 1x oven mitt
- 1x timer
- 1x tweezers or scraping implement
- 2x paper tags indicating sample names
- 2x paper cup for cupcake tray
- Magnetic sediment
- Non-magnetic sediment

B5.2 Process notes

- When sufficiently dry so that the sediment no longer adheres to the sieve, remove from the sieve and place in paper cup for cupcake tray.
- Place one paper cup filled with non-magnetic sediment and one paper cup filled with magnetic sediment in the metal cupcake tray.
- Place metal cupcake tray in the oven set to 135 degrees Celsius, for 30 minutes. Set timer for 30 minutes.
- Move paper tags for each sample to station 4 indicating each sample is now drying in the oven.
- Remove tray from oven using oven mitt after oven firing time has elapsed.

- Transfer tray to Station 4, place on hot pad.
- Optional: using thermal camera, identify hot spots in the sediment which will indicate metallic substances with a higher specific heat. These hot spots are more likely to contain spherules.

B6 BRIDGE LAB: Dry magnetic separation, Station 5

B6.1 Components

- 1x metal tray with raised sides
- 1x small paintbrush, 3mm width
- 1x large paintbrush, 15 mm
- 1x magnetic plunger for dry use
- 1x tweezers with fine point
- 2x paper tags indicating sample names
- 3x sheets of white paper
- Magnetic sediment
- Non-magnetic sediment

B6.2 Process notes

- Remove sediment either from Station 3, sieve drying, or Station 4's cupcake tray and place on separate pieces of white paper, sheets 1 and 2. Do not mix these two samples.
- Move the paper tags indicating the name of each sieve over to Station 5, taking care that each sample's tag is moved to Station 5 correctly.
- Using a marker, label the samples directly on the white sheets of paper 1 and 2 with "[Run Number] Magnetic" and "[Run Number] Non-magnetic". Align paper tags with the sheets of paper.
- Using the tweezers with a fine point, spread out the magnetic sediment on sheet 1. When dry, the sediment should not clump together.
- Using the tweezers with a fine point, spread out the non-magnetic sediment on sheet 2. When dry, the sediment should not clump together.

- Using magnetic plunger for dry use, hover over magnetic sediment on sheet 1, and transfer all magnetic particles to sheet 3. Agitate the magnetic sediment on sheet 1 to change its distribution. Repeat this process until all magnetic particles have been transferred from sheet 1 to sheet 3.
- When all magnetic particles have been transferred to sheet 3, lift sheet 3 and bend the paper to aggregate all magnetic sediment in the center of the sheet.
- Transfer all remaining material on sheet 1 to sheet 2, combining this material with sheet's non-magnetic sediment. (The remnants on sheet 1 are non-magnetic material.)

B7 BRIDGE LAB: Bottling and labeling, Station 6

B7.1 Components

- 1x sheet of paper with Magnetic sediment
- 1x sheet of paper with Non-magnetic sediment
- 1x label maker
- 1x tray for newly created sample vials
- 2x transparent glass vials
- 2x paper tags indicating sample names

B7.2 Process notes

- Fold the sheet of paper with magnetic sediment in half, length-wise.
- Lift the sheet of paper with magnetic sediment and pour the material into a transparent glass vial, using the fold of the paper as a channel to convey the material into the vial.
- Lift the sheet of paper with non-magnetic sediment and pour the material into a transparent glass vial, using the fold of the paper as a channel to convey the material into the vial.
- Create a label with the label maker for the vial now filled with Magnetic sediment, using the naming convention "[Run Number] - MAG" and place the label on the vial.
- Create a label with the label maker for the vial now filled with Non-magnetic sediment, using the naming convention "[Run Number] - NMAG" and place the label on the vial.
- Place both vials in the tray for samples that have yet to be searched (brand new, recently created).
- Move each sample's paper tag from Station 5 to Station 6 to clearly indicate what samples are now ready for examination in the next stage.

B8 BRIDGE LAB: Optical search, Station 7

B8.1 Components

- 1x sample
- 1x Takmlly Digital Microscope USB HD Inspection Camera 50x-1000x displays to laptop
- 2x Elikliv EDM9 7” LCD Digital Microscope 1200X with photographic capacity
- 1x tray for (7A1) samples that have yet to be searched (brand new, recently sorted)
- 1x tray for (7A2) samples that have yet to be searched
- 1x tray for (7B) samples that have been searched
- 1x tray for (7C) new vials containing spherules
- 1x spherule logbook and pencil

B8.2 Process Notes

- Take sample from (7A1) collection of samples that have yet to be searched (brand new, recently sorted) OR (7A2) samples that have yet to be searched to stations with microscope.
- Examine sample under the microscope to look for small spherical objects.
- Remove any spherical, metallic objects above 100 microns and place in separate container.
- Study spherule under another microscope, separately.
- Record diameter of spherule in microns and photograph.
- Place spherule in separate container, label with the following naming convention: "[Run Number - Spherule]".
- Place new vial in tray for (7C) new vials containing spherules.

Appendix C: Preliminary laboratory analysis at UC Berkeley

Scanning Electron Microscope and Energy Dispersive X-Ray Spectroscopy (SEM-EDS) measurements were conducted at UC Berkeley on an initial inventory of spherule samples. A Scios™ 2 DualBeam™ FIB-SEM system was used to provide 3D characterization for the range of samples, including magnetic and non-conductive materials. These samples are dominated by magnetite exteriors with some external and internal dendritic and plate structures, along with various phases and morphology of wustite intergrowths, and complex oxide-alloy interfaces (see Figure C1).

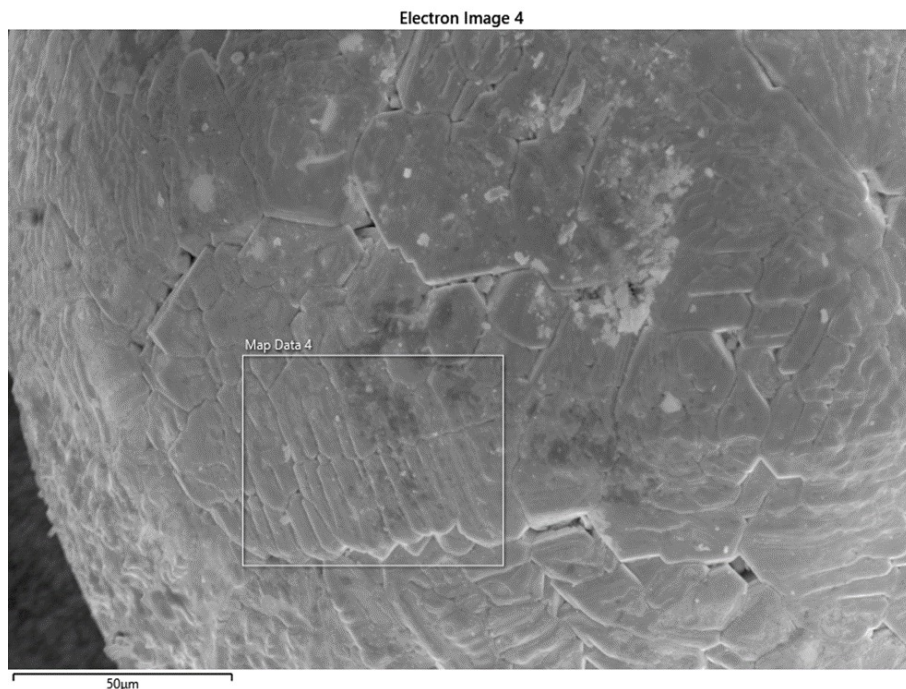


Figure C1. Spherule 14 from run 8, showing full-grown dendritic structure. Different regions show various sizes of grain structure, probably due to differences in the thermal history (solidification rate, grain nucleation).

A single sample collected far away (tens of km) from the IM1 target site contained the largest Ni fraction (0.6% wt), although still much lower than median Ni content for solar system spherules (Genge et al., 2017; Genge et al., 2008; Herzog et al., 1999). For the spherules found inside IM1 search area, the Fe-Mg-Si ratios are consistent with other deep sea and Antarctic spherules (Rochette et al., 2008). Additionally, the SEM/EDS study indicates that many spherules consist of agglomerations of many smaller spherules inside a melted matrix, a behavior consistent with previous studies (Rochette et al., 2008).

In general, dendritic features indicate rapid and heating processes that are consistent with atmospheric entry events. A single sample collected far away (>5km) from the IM1 target site contained the largest Ni fraction (0.6% by weight), which is within the Ni content range for solar system spherules.

The SEM-EDS study indicates that spherules consist of agglomerations of many smaller spherules inside a melted matrix.

Several spherules were found within a much larger (mm-scale) sized irregular shaped Fe-rich matrix, which could indicate a possible precursor terrestrial hydrothermal source, where previous studies have collected magnetite spherules with interlocking plate structures (Agarwal and Palayil, 2022).

A single cross section of a target area spherule did not reveal any dendritic interior structure. On another target area of a spherule (see Figure C4) a line of dendritic ridges indicates Ti-rich and Mn-rich precipitates.



Figure C2. SEM image of Spherule S4 (run 8) showing interior micro-spherules of approximately 5-10 microns in diameter.

During sample processing for SEM analysis, the spherule on the right side of Figure C5 fractured, allowing for an internal morphology (Figure C6) and composition analysis. The EDS mapping of the internal structure revealed extremely high Ti content (>15% by weight), as shown in Figure C7.

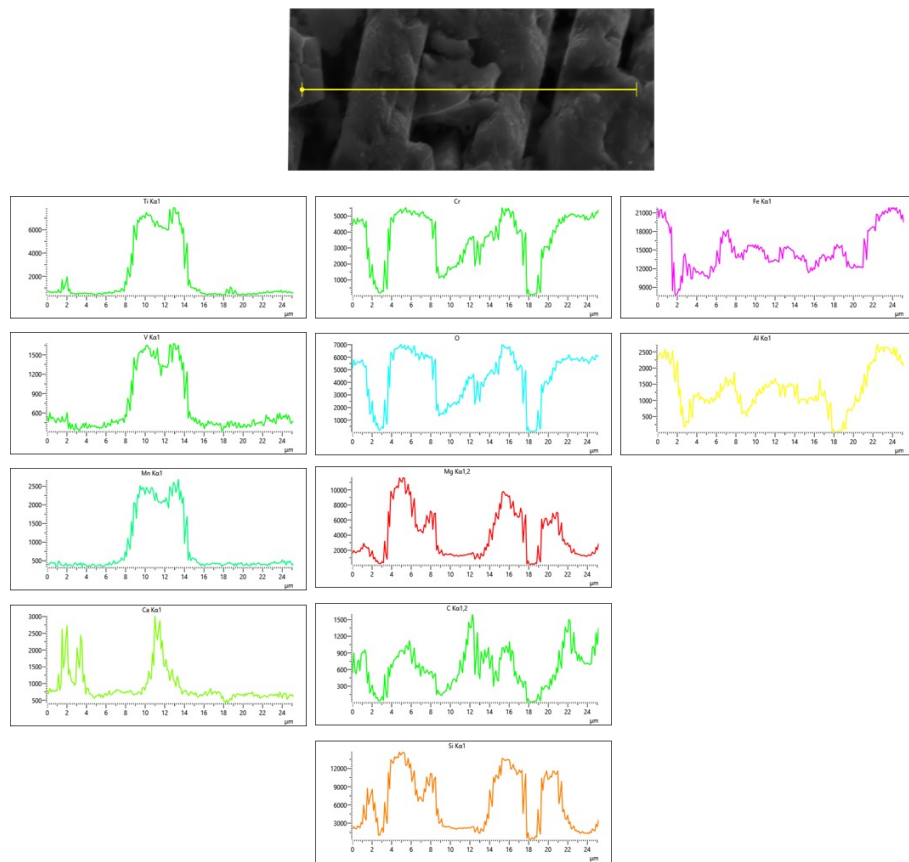


Figure C3. Spherule 14 (run 8), Showing a line-scan EDS analysis across dendritic structures and precipitate composed primarily of Ti with traces of V and Mn.

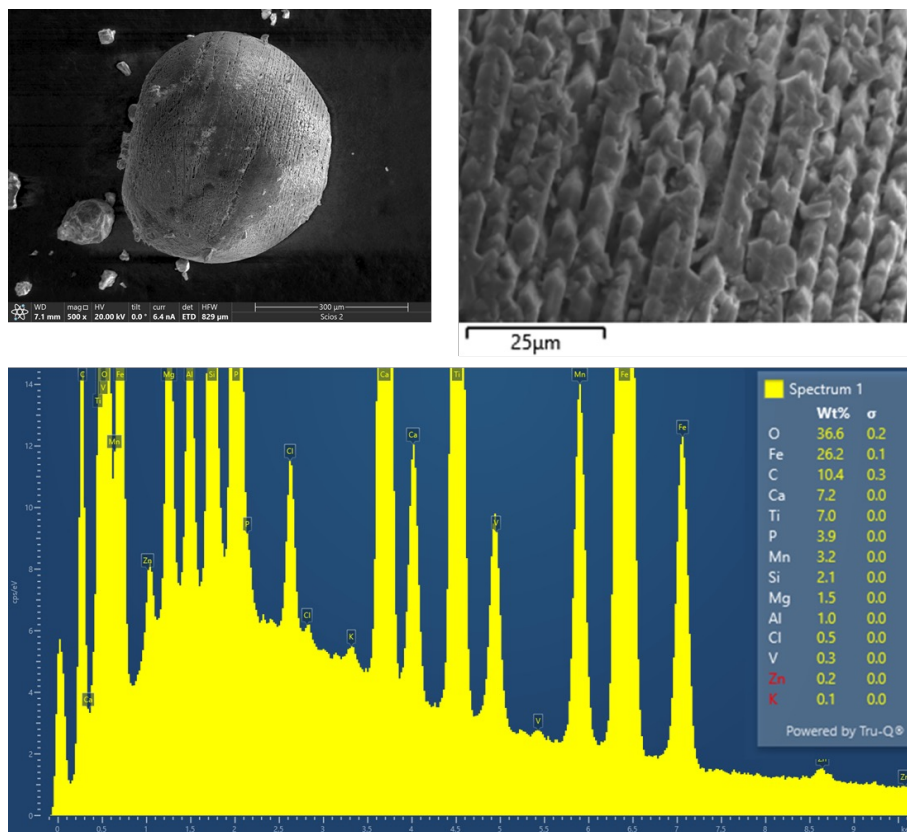


Figure C4. SEM image of Spherule S4 (run 8) showing interior micro-spherules of approximately 5-10 microns in diameter.

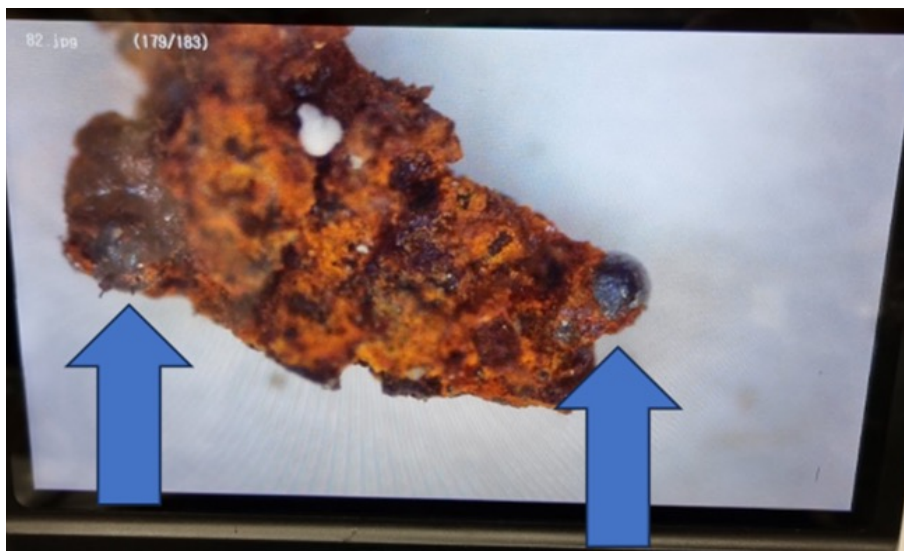


Figure C5. Optical microscope image of a sample collected on run 25, showing an aggregate iron-oxide particle with embedded spherules (blue arrows). The aggregate is approximately 2mm in length

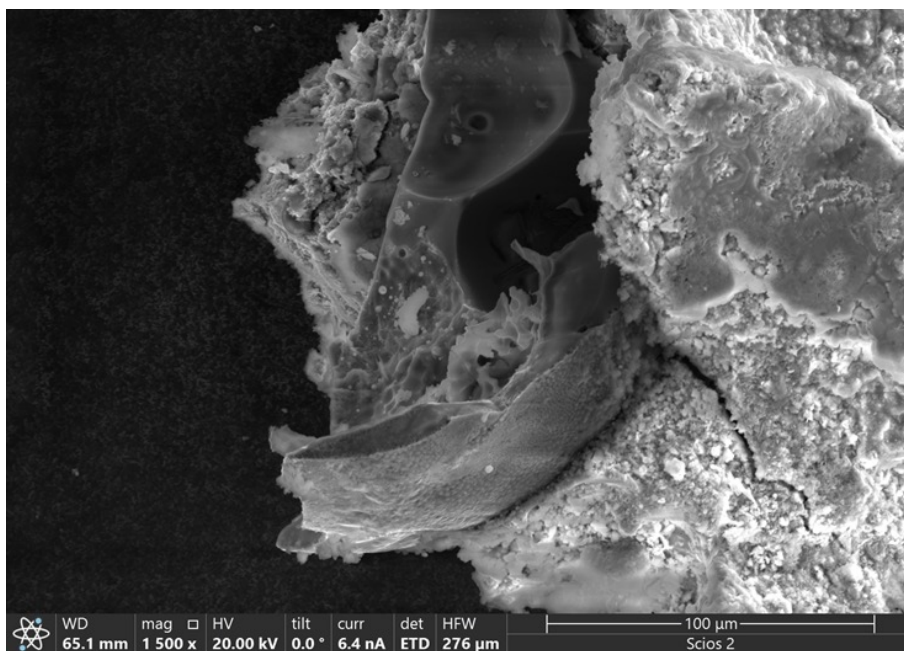


Figure C6. The internal structure of spherule from run 25, embedded in Fe-rich matrix.

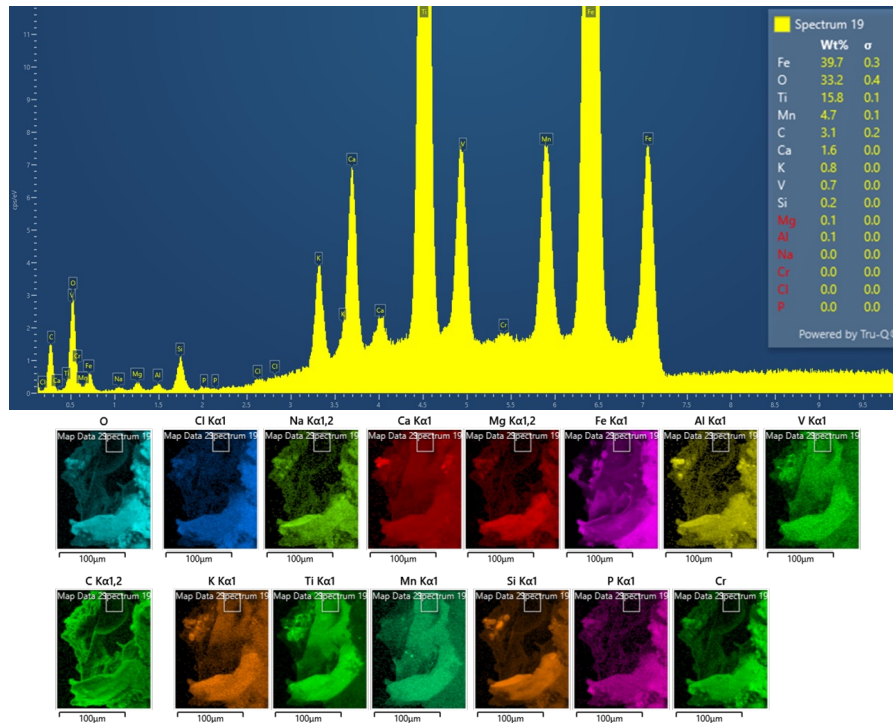


Figure C7. EDS map of fractured spherule from the aggregate matrix acquired on run 25

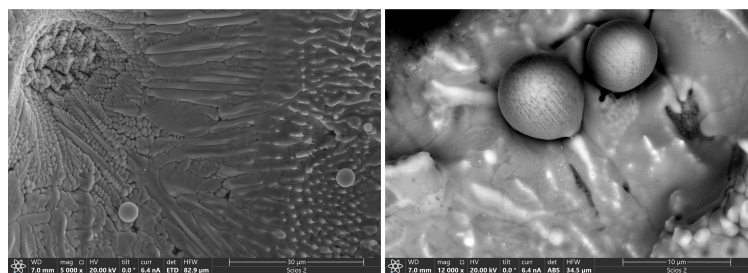


Figure C8. Spherule 4 from run 8 along IM1's path, showing dendritic structure. Note several small spherical particles with fine structure are embedded in the core of larger particles.

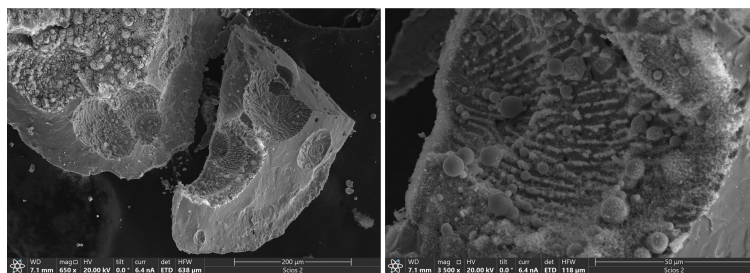


Figure C9. Spherule 4 from run 8, showing many smaller-sized particles embedded in the core of the larger structure.